

Cross-boosting of WNNM Image Denoising method by Directional Wavelet Packets

Amir Averbuch¹ Pekka Neittaanmäki² Valery Zheludev¹ Moshe Salhov¹ Jonathan Hauser³

¹School of Computer Science, ³School of Electrical Engineering
Tel Aviv University, Israel

²Faculty of Mathematical Information Technology
University of Jyväskylä, Finland

Abstract

The paper presents an image denoising scheme by combining a method that is based on directional quasi-analytic wavelet packets (qWPs) with the state-of-the-art Weighted Nuclear Norm Minimization (WNNM) denoising algorithm. The qWP-based denoising method (qWPdn) consists of multiscale qWP transform of the degraded image, application of adaptive localized soft thresholding to the transform coefficients using the *Bivariate Shrinkage* methodology, and restoration of the image from the thresholded coefficients from several decomposition levels. The combined method consists of several iterations of qWPdn and WNNM algorithms in a way that at each iteration the output from one algorithm boosts the input to the other. The proposed methodology couples the qWPdn capabilities to capture edges and fine texture patterns even in the severely corrupted images with utilizing the non-local self-similarity in real images that is inherent in the WNNM algorithm. Multiple experiments, which compared the proposed methodology with six advanced denoising algorithms, including WNNM, confirmed that the combined cross-boosting algorithm outperformed most of them in terms of both quantitative measure and visual perception quality.

1 Introduction

High quality denoising is one of the main challenges in image processing. It tries to achieve suppression of noise while capturing and preserving edges and fine structures in the image. A huge number of publications related to a variety of denoising methods (see, for example the reviews [21, 41, 26]) exist.

Currently, two main groups of image denoising methods exist:

1. “Classical” schemes, which operate on single images;
2. Methodologies based on Deep Learning.

We briefly discuss the relation between these groups of methods in Section 3.4.

Most up to date “classical” schemes, where the proposed algorithm belongs to, are based on one of two approaches.

Utilization of non-local self-similarity (NSS) in images: Starting from the introduction of the Non-local mean (NLM) filter in [7], which is based on the similarity between pixels in

different parts of the image, the exploitation of various forms of the NSS in images has resulted in a remarkable progress in image denoising. It is reflected in multiple publications ([15, 16, 22, 44, 18, 33, 46], to name a very few). The NSS is explored in some denoising schemes based on Deep Learning ([11, 45], for example).

A kind of benchmark in image denoising remains the BM3D algorithm ([15]), which was presented as far as 2007. The algorithm exploits the self-similarity of patches and sparsity of the image in a transform domain. It collects similar patches in the image into a 3D array, which is subjected to a decorrelating 3D transform followed by either hard thresholding or Wiener filtering. After the inverse transforms, the processed patches are returned to their original locations with corresponding weights. This method is highly efficient in restoration of moderately noised images. However, the BM3D tends to over-smooth and smear the image fine structure and edges when noise is strong.

Some improvement of the original BM3D algorithm was achieved by using shape adaptive neighborhoods and the inclusion of the Principal Component Analysis (PCA) into the 3D transform (BM3D-SAPCA algorithm, [16]). Even better results compared to BM3D and BM3D-SAPCA are demonstrated by the so-called Weighted Nuclear Norm Minimization (WNNM) method ([22]), which is based on the assumption that, by stacking the nonlocal similar patch vectors into a matrix, this matrix should be a low rank matrix and, as such, must have sparse singular values. The low rank matrix approximation in [22] is achieved by an adaptive weighted thresholding SVD values of such matrices. Many denoising algorithms presented in recent years, which are based on the NSS concept, report results close to the results produced by BM3D-SAPCA and WNNM. At the same time, they share, to some extent, the shortcomings of the BM3D algorithm, especially blurring the fine structure of images restored from the severely degraded inputs.

Transform domain filtering using directional filters: A way to capture lines, edges and texture pattern while restoring degraded images is to use directional filters and, respectively, dictionaries of waveforms oriented in multiple directions and having an oscillatory structure. A number of dictionaries are reported in the literature and applied to image processing. We mention contourlets [17], curvelets [9, 8], pseudo-polar Fourier transforms [1, 2] and related to them shearlets [31, 20]. However, while these transforms successfully capture edges in images, these dictionaries did not demonstrate a satisfactory texture restoration due to the shortage of oscillating waveforms in the dictionaries.

A number of publications [30, 37, 27, 6, 24, 23, 25, 28, 29], to name a few, derive directional dictionaries by the tensor multiplication of complex wavelets, wavelet frames and wavelet packets (WPs). The tight tensor-product complex wavelet frames (TP_CTF_n)¹ with different numbers of directions, are designed in [24, 25, 23] and some of them, in particular cptTP_CTF₆, TP_CTF₆ and TP_CTF₆[↓], demonstrate impressive performance for image denoising and inpainting. The waveforms in these frames are oriented in 14 directions and, due to the 2-layer structure of their spectra, they possess certain, although limited, oscillatory properties.

In [10] (algorithm *Digital Affine Shear Filter Transform with 2-Layer Structure (DAS-2)*) the two-layer structure, which is inherent in the TP_CTF₆ frames, is incorporated into shearlet-

¹The index n refers to the number of filters in the underlying one-dimensional complex tight framelet filter bank.

based directional filter banks introduced in [47]. This improves the performance of DAS-2 in comparison to TP-CTF_6 on texture-rich images, which is not the case for smoother images.

Recently, we designed a family of complex WPs ([3], brief outlook of the design is in [5]), which are referred to as quasi-analytic WPs (qWPs). As a base for the design, the family of WPs originated from periodic splines of different orders, which are described in [4] (Chapter 4), is used. The two-dimensional (2D) qWPs are derived by a standard tensor products of 1D qWPs. The real parts of the 2D qWPs possess a combination of properties valuable for image processing: They are oriented in multiple directions, (see Table 2.1); The waveforms are close to directional cosine waves with multiple frequencies modulated by localized low-frequency 2D signals; Their DFT spectra form a refined split of the frequency domain; Both one- and two-dimensional qWP transforms are implemented in a very fast ways by using the Fast Fourier transform (FFT). The directional qWPs are successfully applied to image inpainting ([5]).

Due to the above properties, a qWP-based denoising algorithm (qWPdn), which utilizes an adapted version of the Bivariate Shrinkage algorithm (BSA [38, 14]), proved to be efficient for image denoising. Experiments with the qWPdn demonstrate its ability to restore edges and texture details even from severely degraded images. In most experiments, the qWPdn to be described in Section 3.1 provides better resolution of edges and fine structures compared to the cptTP-CTF_6 , DAS-2 and NSS-based algorithms, which is reflected in getting higher Structural Similarity Index (SSIM)² values. On the other hand, the NSS-based algorithms, especially WNNM, proved to be superior in the noise suppression, especially in smooth regions of images, thus producing the highest PSNR values in almost all the experiments. However, some over-smoothing effect on the edges and fine texture persisted under the BM3D, BM3D-SAPCA, NCSR ([18]) and WNNM algorithms. Especially, this is the case for severely degraded images.

Therefore, we propose to combine the qWPdn and WNNM algorithms in order to retain strong features of both algorithms and to get rid of their drawbacks. The combined qWPdn–WNNM algorithms presented in the paper consist of the iterated execution of the qWPdn and WNNM algorithms in a way that at each iteration, the output from one algorithm updates (boosts) the input to the other. Typically, 2–3 (rarely more than 4) iterations are needed to get an excellent result.

In multiple experiments, part of which is reported in Section 3.3, the qWPdn–WNNM algorithms performance is compared with the performance of the NSS-based BM3D, BM3D-SAPCA, NCSR and WNNM algorithms and the algorithms cptTP-CTF_6 and DAS-2 using directional filters. The hybrid qWPdn–WNNM algorithms demonstrated noise suppression efficiency that is quite competitive with all the above methods. It produces PSNR values higher than BM3D produces and either very close to or higher than the values produced by the BM3D-SAPCA, NCSR and WNNM algorithms. On the other hand, its performance related to the edge and fine structures resolution is much better than the performance of all the participated algorithms, thus, producing significantly higher SSIM values.

This observation is illustrated by diagrams in Fig. 1.1. The left frame in Fig. 1.1 shows PSNR values for the restoration of images degraded by Gaussian noise with $\text{STD } \sigma = 5, 10, 25, 40, 50, 80$ and 100 dB , by the above six methods and two combined qWPdn–WNNM algorithms designated by **cbWNNM** and **hybrid**. The PSNR values are averaged over ten images participated in the

²[43], `ssim.m` Matlab 2020b function.

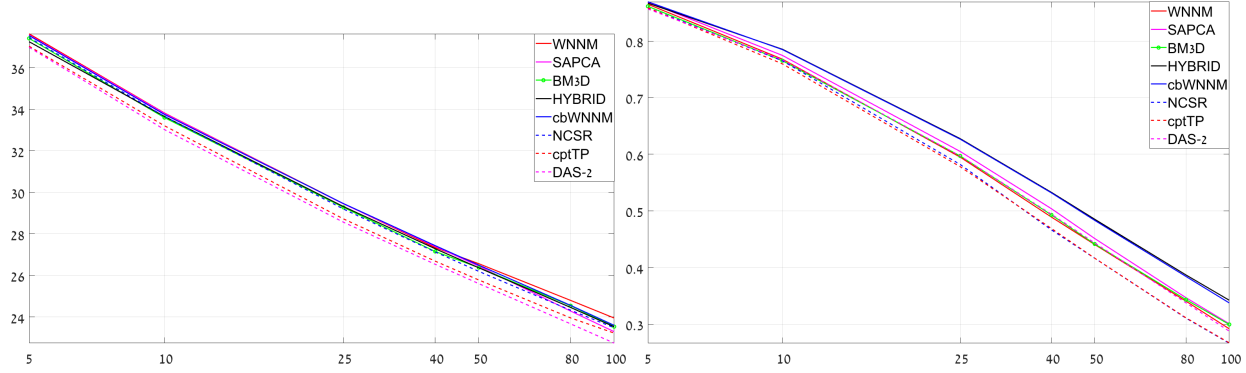


Figure 1.1: Diagrams of PSNR (left frame) and SSIM (right frame) values averaged over ten images for restoration of the images by eight different methods. Labels on x-axes indicate $\text{STD}=\sigma$ values of the additive noise (logarithmic scale)

experiments (see Fig. 3.1). The right frame in Fig. 1.1 does the same for the SSIM values. We can observe that the averaged PSNR values for our methods **cbWNNM** and **hybrid** practically coincide with each other and are very close to the values produced by BM3D-SAPCA and WNNM. A different situation we see in the right frame, which displays averaged SSIM values. Again, the averaged values for our methods **cbWNNM** and **hybrid** practically coincide with each other but they strongly override the values produced by all other methods.

Contribution of the paper:

- Development of fast image denoising algorithm qWPdn based on recently designed directional quasi-analytic wavelet packets.
- Design of the iterative cross-boosting qWPdn–WNNM algorithms, which are highly efficient in noise suppression and capturing edges and fine structures even in severely degraded images.
- Experimental comparison of the qWPdn–WNNM algorithms performance with the performance of multiple state-of-the-art algorithms, which demonstrated a decisive advantage of these algorithms in a SSIM sense and visual perception.

The paper is organised as follows: Section 2 briefly outlines properties of the qWP transforms in one and two dimensions. Section 3.1 describes the qWPdn algorithm. Section 3.2 presents the combined qWPdn–WNNM algorithms. In the multiple experiments in Section 3.3, the performance of these algorithms is compared with the performance of the cptTP– CTF_6 , DAS-2, BM3D, BM3D-SAPCA, NCSR and WNNM algorithms. Section 3.4 briefly discusses the relation of the proposed methodology to the recently published Deep Learning denoising methods. Section 4 provides an overview of the results.

Notation and abbreviations: $N = 2^j$, $\omega \stackrel{\text{def}}{=} e^{2\pi i/N}$ and $\Pi[N]$ is a space of real-valued N -periodic signals. $\Pi[N, N]$ is the space of two-dimensional N -periodic in both vertical and horizontal directions arrays. DFT(FFT) means Discrete(Fast) Fourier transform.

The abbreviations WP, dWP and qWP mean wavelet packet, orthonormal spline-based wavelet packet $\psi_{[m],l}^p$ and quasi-analytic wavelet packets $\Psi_{\pm[m],l}^p$, respectively, in a 1D case, and orthonormal WPs $\psi_{[m],j,l}^p$ and quasi-analytic wavelet packets $\Psi_{\pm\pm[m],l,j}^p$, respectively, in a 2D case.

qWPdn designates the qWP-based image denoising algorithm. qWPdn-WNNM means a cross-boosting image denoising algorithm combining the qWPdn with the BM3D.

PSNR means Peak Signal-to-Noise ratio in decibels (dB). SSIM means Structural Similarity Index ([43]) computed by the Matlab 2020b function `ssim.m`. BSA stands for Bivariate Shrinkage algorithm ([14, 38]). NSS means non-local self-similarity.

BM3D stands for *Block-matching and 3D filtering* ([15]), SAPCA means Shape-Adaptive Principal Component Analysis ([16]), NCSR means Nonlocally Centralized Sparse Representation ([18]), WNNM means Weighted Nuclear Norm Minimization ([22]), cptTP-CTF stands for *Compactly Supported Tensor Product Complex Tight Framelets with Directionality* ([48]) and DAS-2 stands for *Digital Affine Shear Filter Transform with 2-Layer Structure* ([10]).

2 Preliminaries: Quasi-analytic directional wavelet packets

Recently we designed a family of quasi-analytic wavelet packets (qWPs), which possess a collection of properties indispensable for image processing. A brief outline of the qWPs design and the implementation of corresponding transforms is provided the paper [5], which describes successful application of qWPs to image inpainting. A detailed description of the design and implementation is given in [3]. In this section we list properties of qWPs and present some illustrations.

2.1 Properties of qWPs

One-dimentional qWPs The qWPs are derived from the periodic WPs originating from orthonormal discretized polynomial splines of different orders (dWPs), which are described in Chapter 4 in [4] (a brief outline is given in [3]). The dWPs are denoted by $\psi_{[m],l}^p$, where p means the generating spline's order, m is the decomposition level and $l = 0, \dots, 2^m - 1$, is the index of an m -level wavelet packets. The 2^m -sample shifts $\{\psi_{[m],l}^p(\cdot - 2^m k)\}$, $l = 0, \dots, 2^m - 1$, $k = 0, \dots, N/2^m - 1$, of the m -level dWPs form an orthonormal basis of the space $\Pi[N]$ of N -periodic discrete-time signals. Surely, other orthonormal bases are possible, for example, wavelet and Best bases ([12]).

The waveforms $\psi_{[m],l}^p[k]$ are symmetric, well localized in the spatial domain and have oscillatory structure. Their DFT spectra form a refined split of the frequency domain. The shapes of magnitude spectra tend to rectangular as the spline's order p grows. A common way to extend 1D WP transforms to multiple dimensions is by the tensor-product extension. The 2D dWPs from the level m are: $\psi_{[m],j,l}^p[k, n] \stackrel{\text{def}}{=} \psi_{[m],j}^p[k] \psi_{[m],l}^p[n]$. Their 2^m -sample shifts along vertical and horizontal directions form orthonormal bases of the space $\Pi[N, N]$ of 2D signals N -periodic in both directions. The drawback for image processing is the lack of directionality. The directionality can be achieved by switching to complex wavelet packets.

For this, we start with application of the Hilbert transform (HT) to the dWPs $\psi_{[m],l}^p$, thus getting the signals $\tau_{[m],l}^p = H(\psi_{[m],l}^p)$, $m = 1, \dots, M$, $l = 0, \dots, 2^m - 1$. A slight correction of those signals spectra:

$$\hat{\phi}_{[m],l}^p[n] \stackrel{\text{def}}{=} \hat{\psi}_{[m],l}^p[0] + \hat{\psi}_{[m],l}^p[N/2] + \hat{\tau}_{[m],l}^p[n] \quad (2.1)$$

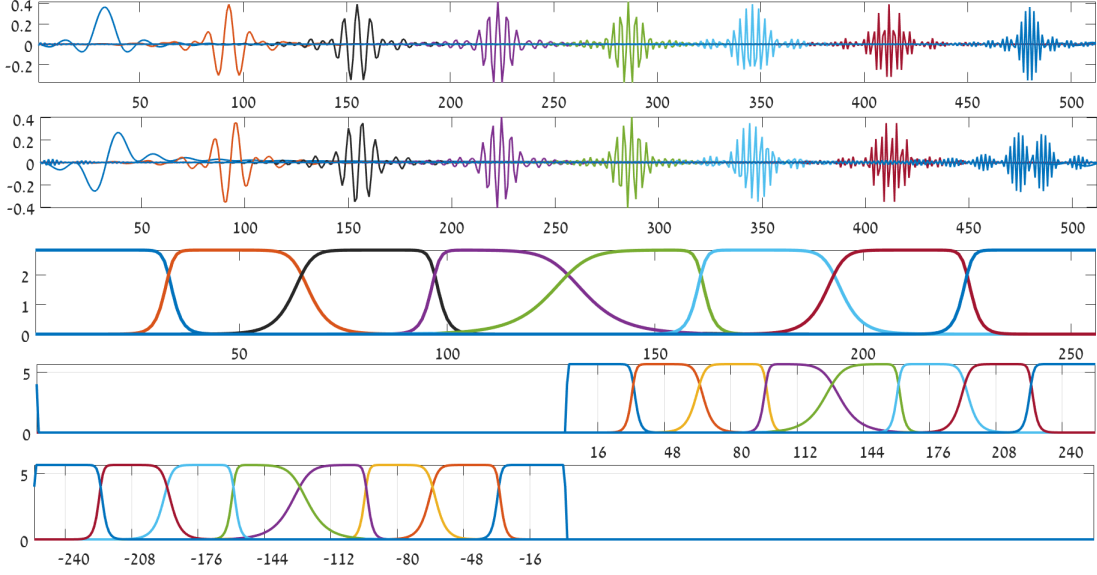


Figure 2.1: Top to bottom: signals $\psi_{[3],l}^9$; signals $\phi_{[3],l}^9$, $l = 0, \dots, 7$; their magnitude DFT spectrum (right half-band); magnitude DFT spectra of complex qWPs $\Psi_{+[3],l}^9$; same for $\Psi_{-[3],l}^9$, $l = 0, \dots, 7$

provides us with a set of signals from the space $\Pi[N]$, whose properties are similar to the properties of the dWPs $\psi_{[m],l}^p$. In particular, their shifts form orthonormal bases in $\Pi[N]$, their magnitude spectra coincide with the magnitude spectra of the dWPs $\psi_{[m],l}^p$. However, unlike the symmetric dWPs $\psi_{[m],l}^p$, the signals $\phi_{[m],l}^p$ are antisymmetric for all l except for $l_0 = 0$ and $l_m = 2^m - 1$. We refer to the signals $\phi_{[m],l}^p$ as the complementary orthonormal WPs (cWPs).

The sets of complex-valued WPs, which we refer to as the quasi-analytic wavelet packets (qWP), are defined as $\Psi_{\pm[m],l}^p \stackrel{\text{def}}{=} \psi_{[m],l}^p \pm i\phi_{[m],l}^p$, $m = 1, \dots, M$, $l = 0, \dots, 2^m - 1$, where $\phi_{[m],l}^p$ are the cWPs defined in Eq. (2.1). The qWPs $\Psi_{\pm[m],l}^p$ differ from the analytic WPs by adding two values $\pm i\hat{\psi}_{[m],l}^p[0]$ and $\pm i\hat{\psi}_{[m],l}^p[N/2]$ into their DFT spectra, respectively. The DFT spectra of the qWPs $\Psi_{+[m],l}^p$ are located within positive half-band of the frequency domain and vice versa for the qWPs $\Psi_{-[m],l}^p$.

Figure 2.1 displays the signals $\psi_{[3],l}^9$ and $\phi_{[3],l}^9$, $l = 0, \dots, 7$, from the third decomposition level and their magnitude spectra (right half-band), that coincide with each other. Addition of $\hat{\psi}_{[3],l}^9[0]$ and $\hat{\psi}_{[3],l}^9[N/2]$ to the spectra of $\phi_{[3],l}^9$, $l = 0, 7$, results in an antisymmetry distortion. These WPs provide a collection of diverse symmetric and antisymmetric well localized waveforms, which range from smooth wavelets for $l = 0, 1$ to fast oscillating transients for $l = 5, 6, 7$. Thus, this collection is well suited to catching smooth as well as oscillating local patterns in signals. In the 2D case, these valuable properties of the spline-based wavelet packets are completed by the directionality of the tensor-product waveforms.

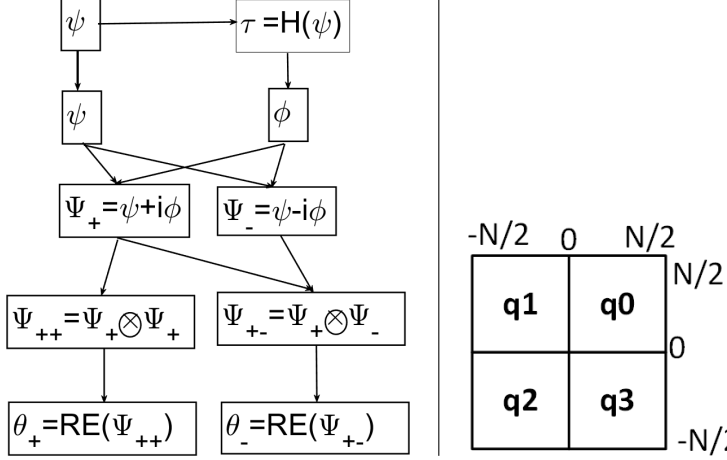


Figure 2.2: Block-scheme of the qWP design (left) and quadrants of frequency domain (right)

Two-dimensional qWPs Similarly to the 2D dWPs $\psi_{[m],j,l}^p[k, n]$, the 2D cWPs $\phi_{[m],j,l}^p[k, n]$ are defined as the tensor products of 1D WPs such that $\phi_{[m],j,l}^p[k, n] \stackrel{\text{def}}{=} \phi_{[m],j}^p[k] \phi_{[m],l}^p[n]$. The 2^m -sample shifts of the WPs $\{\phi_{[m],j,l}^p\}$, $j, l = 0, \dots, 2^m - 1$, in both directions form an orthonormal basis for the space $\Pi[N, N]$ of arrays that are N -periodic in both directions.

2D qWPs and their spectra The 2D dWPs $\{\psi_{[m],j,l}^p\}$ as well as the cWPs $\{\phi_{[m],j,l}^p\}$ lack the directionality property which is needed in many applications that process 2D data. However, real-valued 2D wavelet packets oriented in multiple directions can be derived from tensor products of complex quasi-analytic qWPs $\Psi_{\pm[m],\rho}^p$. The complex 2D qWPs are defined as follows:

$$\Psi_{++[m],j,l}^p[k, n] \stackrel{\text{def}}{=} \Psi_{+[m],j}^p[k] \Psi_{+[m],l}^p[n], \quad \Psi_{+-[m],j,l}^p[k, n] \stackrel{\text{def}}{=} \Psi_{+[m],j}^p[k] \Psi_{-[m],l}^p[n], \quad (2.2)$$

where $m = 1, \dots, M$, $j, l = 0, \dots, 2^m - 1$, and $k, n = 0, \dots, N - 1$. The real parts of these 2D qWPs are

$$\begin{aligned} \theta_{+[m],j,l}^p[k, n] &\stackrel{\text{def}}{=} \Re(\Psi_{++[m],j,l}^p[k, n]) = \psi_{[m],j,l}^p[k, n] - \phi_{[m],j,l}^p[k, n], \\ \theta_{-[m],j,l}^p[k, n] &\stackrel{\text{def}}{=} \Re(\Psi_{+-[m],j,l}^p[k, n]) = \psi_{[m],j,l}^p[k, n] + \phi_{[m],j,l}^p[k, n]. \end{aligned} \quad (2.3)$$

The block-scheme in Fig. 2.2 illustrates the design of qWPs. The DFT spectra of the 2D qWPs $\Psi_{++[m],j,l}^p$, $j, l = 0, \dots, 2^m - 1$, are tensor products of the one-sided spectra of the qWPs $\hat{\Psi}_{++[m],j,l}^p[p, q] = \hat{\Psi}_{+[m],j}^p[p] \hat{\Psi}_{+[m],l}^p[q]$ and, as such, they fill the quadrant \mathbf{q}_0 of the frequency domain, while the spectra of $\Psi_{+-[m],j,l}^p$, $j, l = 0, \dots, 2^m - 1$, fill the quadrant \mathbf{q}_1 (see Fig. 2.2). Figure 2.3 displays magnitude spectra of the ninth-order 2D qWPs $\Psi_{++[2],j,l}^9$ and $\Psi_{+-[2],j,l}^9$ from the second decomposition level. Figure 2.3 shows that the DFT spectra of the qWPs $\Psi_{\pm[m],j,l}^9$ effectively occupy relatively small squares in the frequency domain. For deeper decomposition levels, sizes of the corresponding squares decrease as geometric progression. Such configuration of the spectra leads to the directionality of the real-valued 2D WPs $\theta_{\pm[m],j,l}^p$. The directionality of the WPs $\theta_{\pm[m],j,l}^p$ is discussed in [3]. It is established that if the spectrum of a WP $\Psi_{\pm[m],j,l}^p$ occupies a square whose center lies in the point $[\kappa_0, \nu_0]$, then the respective real-valued WP $\theta_{\pm[m],j,l}^p$ defined in Eq. (2.3) is represented by $\theta_{\pm[m],j,l}^p[k, n] \approx \cos \frac{2\pi(\kappa_0 k + \nu_0 n)}{N} \underline{\theta}[k, n]$, where $\underline{\theta}[k, n]$ is a spatially localized

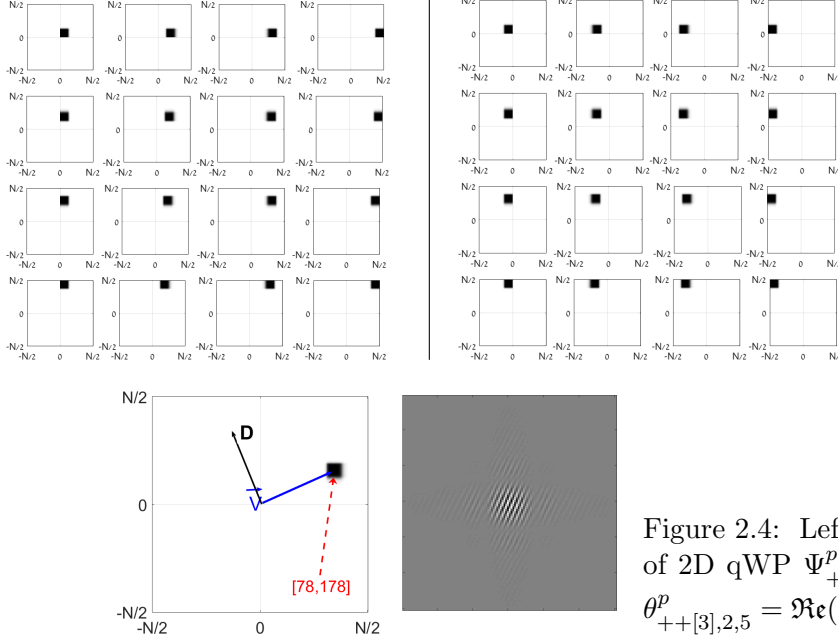


Figure 2.3: Magnitude spectra of 2D qWPs $\Psi_{++[2],j,l}^9$ (left) and $\Psi_{--[2],j,l}^9$ (right) from the second decomposition level

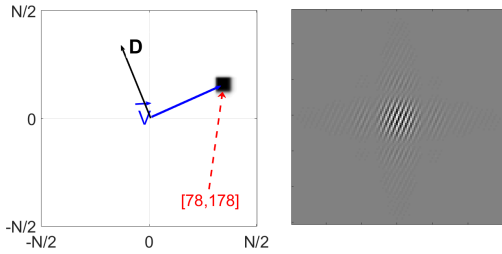


Figure 2.4: Left: magnitude spectrum of 2D qWP $\Psi_{++[3],2,5}^p[k, n]$. Right WP $\theta_{++[3],2,5}^p = \Re(\Psi_{++[3],2,5}^p)$

low-frequency waveform which does not have a directionality. But the 2D signal $\cos \frac{2\pi(\kappa_0 k + \nu_0 n)}{N}$ is oscillating in the direction \mathbf{D} , which is orthogonal to the vector $\vec{V} = \kappa_0 \vec{i} + \nu_0 \vec{j}$. Therefore, WP $\theta_{\pm[m],j,l}^p$ can be regarded as the directional cosine wave modulated by the localized low-frequency signal θ . The cosine frequencies in the vertical and horizontal directions are determined by the indices j and l , respectively, of the WP $\theta_{\pm[m],j,l}^p$. The bigger is the index, the higher is frequency in the respective direction. The situation is illustrated in Fig. 2.4. The imaginary parts of the qWPs $\Psi_{\pm[m],j,l}^p$ have a similar structure.

Figure 2.5 displays WPs $\theta_{+[2],j,l}^9$, $j, l = 0, 1, 2, 3$, from the second decomposition level and their magnitude spectra.

Figure 2.6 displays WPs $\theta_{-[2],j,l}^9$, $j, l = 0, 1, 2, 3$, from the second decomposition level and their magnitude spectra.

Figure 2.7 displays WPs $\theta_{+[3],j,l}^9$ and $\theta_{-[3],j,l}^9$, $j, l = 0, 1, 2, 3$, from the third decomposition level.

Remark 2.1 Note that all the WPs $\theta_{\pm[m],j,l}^p$ whose spectra are located along the vector \vec{V} have approximately the same orientation. It is seen in Figs. 2.6, 2.5 and 2.7. Consequently, the number of orientations of the m -th level WPs is less than the number of WPs, which is $2 \cdot 4^m$. For example, all the “diagonal” qWPs $\{\theta_{\pm[m],j,j}^p\}$, $j = 0, \dots, 2^m - 1$, are oscillating with different frequencies in the directions of either 135° (for θ_+) or 45° (for θ_-). Orientation numbers are given in Table 2.1.

2.2 Outline of the implementation scheme for 2D qWP transforms

The spectra of 2D qWPs $\{\Psi_{++[m],j,l}^p\}$, $j, l = 0, \dots, 2^m - 1$ fill the quadrant \mathbf{q}_0 of the frequency domain (see Fig. 2.2), while the spectra of 2D qWPs $\{\Psi_{--[m],j,l}^p\}$ fill the quadrant \mathbf{q}_1 . Consequently,

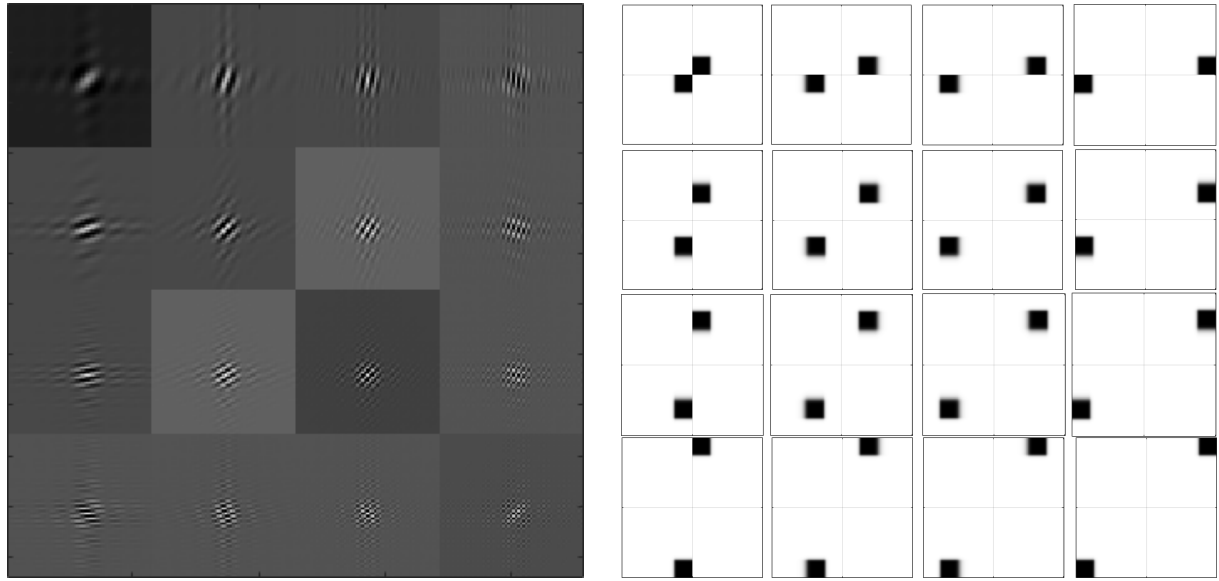


Figure 2.5: WPs $\theta_{+[2],j,l}^9$ from the second decomposition level and their magnitude spectra

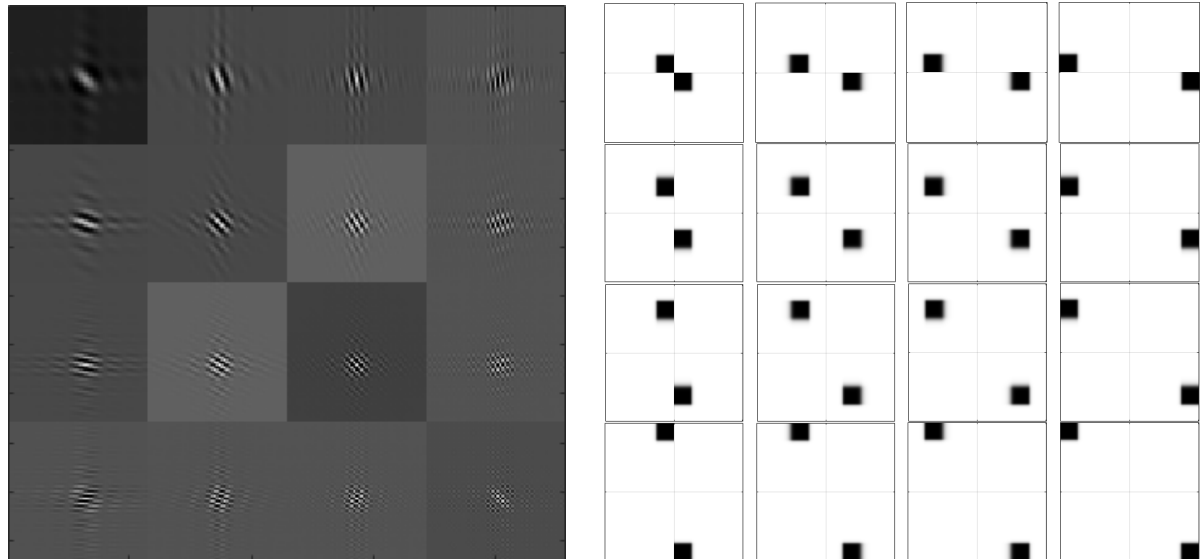


Figure 2.6: WPs $\theta_{-[2],j,l}^9$ from the second decomposition level and their magnitude spectra

Table 2.1: Numbers of different orientations of qWPs $\left\{ \theta_{\pm[m],j,l}^p \right\}$, $j, l = 0, \dots, 2^m - 1$, for different decomposition levels

level m	1	2	3	4	5	6	...
# of directions	6	22	86	318	1290	5030	...

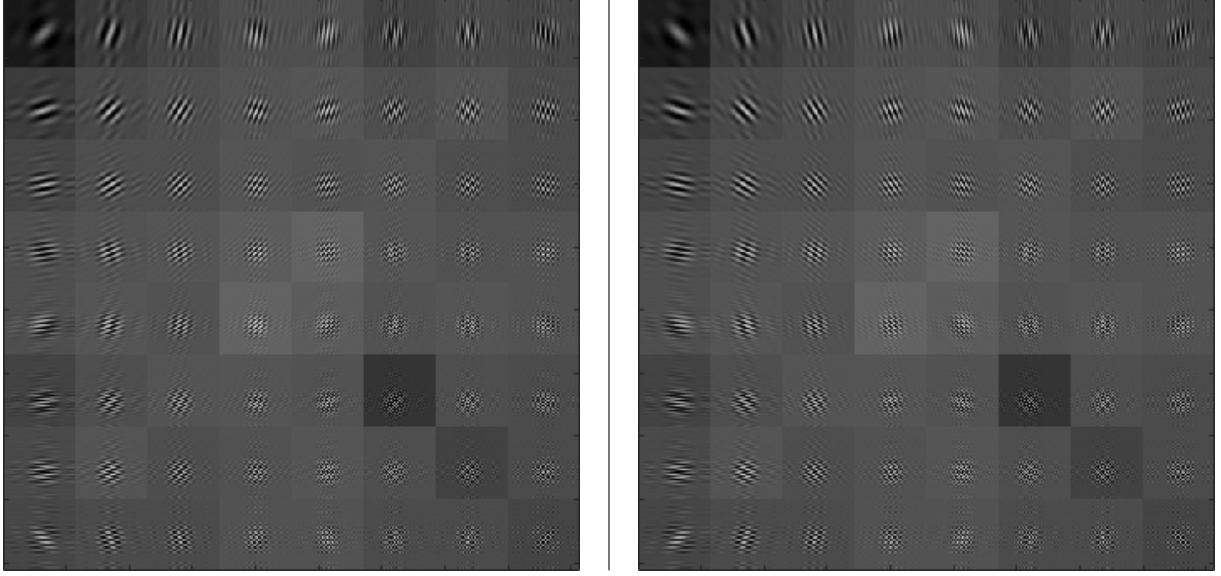


Figure 2.7: WPs $\theta_{+[3],j,l}^9$ (left) and $\theta_{-[3],j,l}^9$ (right) from the third decomposition level

the spectra of the real-valued 2D WPs $\{\theta_{+[m],j,l}^p\}$, $j, l = 0, \dots, 2^m - 1$, and $\{\theta_{-[m],j,l}^p\}$ fill the pairs of quadrant $\mathbf{q}_+ = \mathbf{q}_0 \cup \mathbf{q}_2$ and $\mathbf{q}_- = \mathbf{q}_1 \cup \mathbf{q}_3$, respectively.

By this reason, none linear combination of the WPs $\{\theta_{+[m],j,l}^p\}$ and their shifts can serve as a basis for the signal space $\Pi[N, N]$. The same is true for WPs $\{\theta_{-[m],j,l}^p\}$. However, combinations of the WPs $\{\theta_{+[m],j,l}^p\}$ and $\{\theta_{-[m],j,l}^p\}$ provide frames of the space $\Pi[N, N]$.

The transforms are implemented in the frequency domain using modulation matrices of the filter banks, which are built from the corresponding wavelet packets. It is important to mention that the structure of the filter banks \mathbf{Q}_+ and \mathbf{Q}_- for the first decomposition level is different for the transforms with the “positive” $\Psi_{+[m],l}^p$ and “negative” $\Psi_{-[m],l}^p$ qWPs, respectively. However, the transforms from the first to the second and further decomposition levels are executed using the same filter bank \mathbf{H}_m for the “positive” and “negative” qWPs. This fact makes it possible a parallel implementation of the transforms.

The one-level 2D qWP transforms of a signal $\mathbf{X} = \{X[k, n]\} \in \Pi[N, N]$ are implemented by a tensor-product scheme. To be specific, for the transform with $\Psi_{++[1]}^p$, the 1D transform of rows from the signal \mathbf{X} is executed using the filter bank \mathbf{Q}_+ , which is followed by the 1D transform of columns of the produced coefficient arrays using the same filter bank \mathbf{Q}_+ . These operations result in the transform coefficient array $\mathbf{Z}_{+[1]} = \bigcup_{j,l=0}^1 \mathbf{Z}_{+[1]}^{j,l}$ comprising of four blocks of size $N/2 \times N/2$. The transform with $\Psi_{+-[1]}^p$ is implemented by the subsequent application of the filter banks \mathbf{Q}_+ and \mathbf{Q}_- to rows from the signal \mathbf{X} and columns of the produced coefficient arrays, respectively. This results in the coefficient array $\mathbf{Z}_{-[1]} = \bigcup_{j,l=0}^1 \mathbf{Z}_{-[1]}^{j,l}$.

The further transforms starting from the arrays $\mathbf{Z}_{+[1]}$ and $\mathbf{Z}_{-[1]}$ produce two sets of the coefficients $\{\mathbf{Z}_{+[m]} = \bigcup_{j,l=0}^{2^m-1} \mathbf{Z}_{+[m]}^{j,l}\}$ and $\{\mathbf{Z}_{-[m]} = \bigcup_{j,l=0}^{2^m-1} \mathbf{Z}_{-[m]}^{j,l}\}$, $m = 2, \dots, M$. The transforms are implemented by the application of the same filter banks \mathbf{H}_m , $m = 2, \dots, M$ to rows and columns

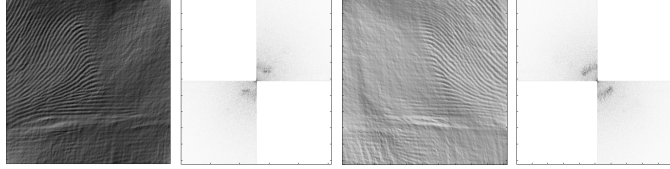


Figure 2.8: Left to right: 1. Image $\Re(\mathbf{X}_+)$. 2. Its magnitude DFT spectrum. 3. Image $\Re(\mathbf{X}_-)$. 4. Its magnitude DFT spectrum

of the “positive” and “negative” coefficient arrays. The coefficients from a level m comprise of 4^m “positive” blocks of coefficients $\{\mathbf{Z}_{+[m]}^{j,l}\}$, $l, j = 0, \dots, 2^m - 1$, and the same number of “negative” blocks $\{\mathbf{Z}_{-[m]}^{j,l}\}$.

The coefficients from a block are inner products of the signal $\mathbf{X} = \{X[k, n]\} \in \Pi[N, N]$ with the shifts of the corresponding wavelet packet:

$$\begin{aligned} Z_{\pm[m]}^{j,l}[k, n] &= \sum_{\lambda, \mu=0}^{N-1} X[\lambda, \mu] \Psi_{\pm[m], j, l}^p[\lambda - 2^m k, \mu - 2^m n], \\ Y_{\pm[m]}^{j,l}[k, n] &= \Re(Z_{\pm[m]}^{j,l}[k, n]) = \sum_{\lambda, \mu=0}^{N-1} X[\lambda, \mu] \theta_{\pm[m], j, l}^p[\lambda - 2^m k, \mu - 2^m n]. \end{aligned} \quad (2.4)$$

The inverse transforms are implemented accordingly. Prior to the reconstruction, some structures, possibly different, are defined in the sets $\{\mathbf{Z}_{+[m]}^{j,l}\}$ and $\{\mathbf{Z}_{-[m]}^{j,l}\}$, $m = 1, \dots, M$, (for example, 2D wavelet, Best Basis or single-level structures) and some manipulations on the coefficients, (for example, thresholding, shrinkage, l_1 minimization) are executed. The reconstruction produces two complex arrays \mathbf{X}_+ and \mathbf{X}_- . The signal \mathbf{X} is restored by $\tilde{\mathbf{X}} = \Re(\mathbf{X}_+ + \mathbf{X}_-)/8$.

Figure 2.8 illustrates the image “Fingerprint” restoration by the 2D signals $\Re(\mathbf{X}_\pm)$. The signal $\Re(\mathbf{X}_-)$ captures oscillations oriented to *north-east*, while $\Re(\mathbf{X}_+)$ captures oscillations oriented to *north-west*. The signal $\tilde{\mathbf{X}} = \Re(\mathbf{X}_+ + \mathbf{X}_-)/8$ perfectly restores the image achieving PSNR=312.3538 dB.

3 Image denoising

In this section, we describe application of the directional qWP transforms presented in Section 2 to the restoration of an image \mathbf{X} from the data $\tilde{\mathbf{X}} = \mathbf{X} + \mathbf{E}$, where \mathbf{E} is the Gaussian zero-mean noise whose STD= σ .

3.1 Denoising scheme for 2D qWPs

The degraded image $\tilde{\mathbf{X}}$ is decomposed into two sets $\{\check{\mathbf{Z}}_{+[m]}^{j,l}\}$ and $\{\check{\mathbf{Z}}_{-[m]}^{j,l}\}$, $m = 1, \dots, M$, $j, l = 0, 2^m - 1$, of the qWP transform coefficients, then a version of the Bivariate Shrinkage algorithm (BSA)[38, 14] is implemented and the image $\tilde{\mathbf{X}} \approx \mathbf{X}$ is restored from the shrunken coefficients. The restoration is executed separately from the sets of coefficients belonging to several decomposition levels and the results are averaged with some weights.

3.1.1 Image restoration from a single-level transform coefficients

Consider the reconstruction of an image $\mathbf{X} \in \Pi[N, N]$ from the fourth-level transform coefficients of the degraded array $\tilde{\mathbf{X}}$ of size $N \times N$.

The denoising algorithm, which we refer to as qWPdn, is implemented by the following steps:

1. In order to eliminate boundary effects, the degraded image $\check{\mathbf{X}}$ is symmetrically extended to the image $\check{\mathbf{X}}_T$ of size $N_T \times N_T$, where $N_T = N + 2T$. Typically, either $T = N/4$ or $T = N/8$.
2. The Bivariate Shrinkage (BSA) utilizes the interscale dependency of the transform coefficients. Therefore, the direct 2D transforms of the image $\check{\mathbf{X}}_T$ with the complex qWPs Ψ_{++}^p and Ψ_{+-}^p are executed down to the fifth decomposition level. As a result, two sets $\check{\mathbf{Z}}_{+[m]}^{j,l} = \{\check{Z}_{+[m]}^{j,l}[k,n]\}$ and $\check{\mathbf{Z}}_{-[m]}^{j,l} = \{\check{Z}_{-[m]}^{j,l}[k,n]\}$, $m = 1, \dots, 5$, $j, l = 0, \dots, 2^m - 1$, $k, n = 0, \dots, N_T/2^m - 1$, of the qWP transform coefficients are produced.

3. The noise variance is estimated by $\tilde{\sigma}_e^2 = \frac{\text{median}(|\check{Z}_{+[1]}^{1,1}[k,n]|)}{0.6745}$.
4. Let $\check{c}_4[k,n] \stackrel{\text{def}}{=} \check{Z}_{+[4]}^{j,l}[k,n]$ denote a coefficient from a block $\check{\mathbf{Z}}_{+[4]}^{j,l}$ at the fourth decomposition level. The following operations are applied to the coefficient $\check{c}_4[k,n]$:

- (a) The averaged variance $\bar{\sigma}_c[k,n]^2 = \frac{1}{W_4^2} \sum_{\kappa, \nu=-W_4/2}^{W_4/2-1} \check{c}_4[k+\kappa, n+\nu]^2$ is calculated. The integer W_4 determines the neighborhood of $\check{c}_4[k,n]$ size.
- (b) The marginal variance for $\check{c}_4[k,n]$ is estimated by $\tilde{\sigma}[k,n]^2 = (\bar{\sigma}_c[k,n]^2 - \tilde{\sigma}_e^2)_+$.³
- (c) In order to estimate the clean transform coefficients from the fourth decomposition level, coefficients from the fifth level should be utilized. The size of the coefficient block $\check{\mathbf{Z}}_{+[4]}^{j,l}$ is $N_T/16 \times N_T/16$. The coefficients from that block are related to the qWP $\Psi_{++[4],j,l}^p$, whose spectrum occupies, approximately, the square $\mathbf{S}_{+[4]}^{j,l}$ of size $N_T/32 \times N_T/32$ within the quadrant \mathbf{q}_0 (see Fig. 2.2). The spectrum's location determines the directionality of the waveform $\Psi_{++[4],j,l}^p$. On the other hand, four coefficient blocks $\{\check{\mathbf{Z}}_{+[5]}^{2j+\iota,2l+\lambda}\}$, $\iota, \lambda = 0, 1$, of size $N_T/32 \times N_T/32$ are derived by filtering the block $\check{\mathbf{Z}}_{+[4]}^{j,l}$ coefficients followed by downsampling. The coefficients from those blocks are related to the qWPs $\Psi_{++[5],2j+\iota,2l+\lambda}^p$, whose spectra occupy, approximately, the squares $\mathbf{S}_{+[5]}^{2j+\iota,2l+\lambda}$ of size $N_T/64 \times N_T/64$, which fill the square $\mathbf{S}_{+[4]}^{j,l}$. Therefore, the orientations of the waveforms $\Psi_{++[5],2j+\iota,2l+\lambda}^p$ are close to the orientation of $\Psi_{++[4],j,l}^p$. Keeping this in mind, we form the joint fifth-level array $\mathbf{c}_5^{j,l}$ of size $N_T/16 \times N_T/16$ by interleaving the coefficients from the arrays $\{\check{\mathbf{Z}}_{+[5]}^{2j+\iota,2l+\lambda}\}$. To be specific, the joint array $\mathbf{c}_5^{j,l}$ consists of the quadruples:

$$\mathbf{c}_5^{j,l} = \left\{ \begin{bmatrix} \check{Z}_{+[5]}^{2j,2l}[\kappa, \nu] & \check{Z}_{+[5]}^{2j,2l+1}[\kappa, \nu] \\ \check{Z}_{+[5]}^{2j+1,2l}[\kappa, \nu] & \check{Z}_{+[5]}^{2j+1,2l+1}[\kappa, \nu] \end{bmatrix} \right\}, \quad \kappa, \nu = 0, \dots, N_T/32 - 1.$$

- (d) Let $\check{c}_5[k,n]$ denote a coefficient from the joint array $\mathbf{c}_5^{j,l}$. Then, the transform coefficient $Z_{+[4]}^{j,l}[k,n]$ from the fourth decomposition level is estimated by the bivariate shrinkage of the coefficients $\check{Z}_{+[4]}^{j,l}[k,n]$:

$$Z_{+[4]}^{j,l}[k,n] \approx \check{Z}_{+[4]}^{j,l}[k,n] = \frac{\left(\sqrt{\check{c}_4[k,n]^2 + \check{c}_5[k,n]^2} - \frac{\sqrt{3}\tilde{\sigma}_e^2}{\tilde{\sigma}[k,n]} \right)_+ \check{c}_4[k,n]}{\sqrt{\check{c}_4[k,n]^2 + \check{c}_5[k,n]^2}}$$

³ $s_+ \stackrel{\text{def}}{=} \max\{s, 0\}$.

5. As a result of the above operations, the fourth-level coefficient array $\tilde{\mathbf{Z}}_{+[4]} = \left\{ \tilde{\mathbf{Z}}_{+[4],j,l} \right\}, j, l = 0, \dots, 15$, is estimated, where $\tilde{\mathbf{Z}}_{+[4],j,l} = \left\{ \tilde{Z}_{+[4]}^{j,l}[k, n] \right\}, k, n = 0, \dots, N_T/16 - 1$.
6. The inverse qWP transform is applied to the coefficient array $\tilde{\mathbf{Z}}_{+[4]}$ and the result shrinks to the original image size $N \times N$. Thus, the sub-image $\tilde{\mathbf{X}}_+^4$ is obtained.
7. The same operations are applied to $\tilde{\mathbf{Z}}_{-[m]}^{j,l}, m = 4, 5$, thus resulting in the sub-image $\tilde{\mathbf{X}}_-^4$.
8. The clean image is estimated by $\mathbf{X} \approx \tilde{\mathbf{X}}^4 = \frac{\Re(\tilde{\mathbf{X}}_+^4 + \tilde{\mathbf{X}}_-^4)}{8}$.

3.1.2 Image restoration from several decomposition levels

More stable estimation of the image \mathbf{X} is derived by the weighted average of several single-level estimations $\left\{ \tilde{\mathbf{X}}^m \right\}$. In most cases, the estimations from the second, third and fourth levels are combined, so that $m = 2, 3, 4$.

The approximated image $\tilde{\mathbf{X}}^3$ is derived from the third-level coefficients $\tilde{\mathbf{Z}}_{\pm[3]}^{j,l}$. The fourth-level coefficients that are needed for the Bivariate Shrinkage of the coefficients $\tilde{\mathbf{Z}}_{\pm[3]}^{j,l}$ are taken from the “cleaned” arrays $\tilde{\mathbf{Z}}_{\pm[4],j,l}$ rather than from the “raw” ones $\tilde{\mathbf{Z}}_{\pm[4],j,l}$.

Similarly, the image $\tilde{\mathbf{X}}^2$, is derived from the coefficient arrays $\tilde{\mathbf{Z}}_{\pm[2]}^{j,l}$ and $\tilde{\mathbf{Z}}_{\pm[3]}^{j,l}$. The final operation is the weighted averaging such as

$$\tilde{\mathbf{X}} = \frac{\alpha_2 \tilde{\mathbf{X}}^2 + \alpha_3 \tilde{\mathbf{X}}^3 + \alpha_4 \tilde{\mathbf{X}}^4}{\alpha_2 + \alpha_3 + \alpha_4}. \quad (3.1)$$

Remark 3.1 *Matlab implementation of all the operations needed to transform the degraded array $\check{\mathbf{X}}$ of size 512×512 into the estimation $\tilde{\mathbf{X}}$ given by Eq. (3.1) takes 1 second. Note that the noise STD is not a part of the input. It is evaluated as indicated in Item 3.*

Remark 3.2 *In some cases, restoration from third, fourth and fifth levels is preferable. Then, the degraded array $\check{\mathbf{X}}_T$ is decomposed down to the sixth level.*

Remark 3.3 *The algorithm comprises a number of free parameters which enable a flexible adaptation to the processed class of objects. These parameters are the order “p” of the generating spline, integers W_4 , W_3 and W_2 , which determine the sizes of neighborhoods for the averaged variances calculation, and the weights α_2 , α_3 and α_4 .*

Remark 3.4 *Fragments of the Matlab functions `denoising_dwt.m` and `bishrink.m` from the web-sites http://eeweb.poly.edu/iselesni/WaveletSoftware/denoising_dwt.html and <http://eeweb.poly.edu/iselesni/WaveletSoftware/denoise2.html>, respectively, were used as patterns while compiling our own denoising software.*

3.2 qWPdn–WNNM: Hybrid algorithm

Equations (2.4) imply that the coefficients of the qWP transforms reflect the correlation of the image under processing with the collection of waveforms, which are well localized in the spatial

domain and are oscillating in multiple directions with multiple frequencies. By this reason, these transforms are well suited for capturing edges and texture patterns oriented in different directions. Experiments with the qWPdn image denoising algorithm demonstrate its ability to restore edges and texture details even from severely degraded images. In most conducted experiments, the qWPdn provides better resolution of edges and fine structures compared to the most state-of-the-art algorithms based on non-local self-similarity (NSS), including the BM3D, NCSR and WNNM algorithms, which is reflected in higher SSIM values. On the other hand, the NSS-based algorithms proved to be superior in noise suppression especially in smooth regions in images, thus producing the high PSNR values.

One of the best existing denoising algorithms is WNNM ([22]) introduced in 2014. It produces high PSNR and SSIM values and, in most cases, a better visual perception of restored images compared to other algorithms. WNNM is an iterative image denoising algorithm, whose main components are stacking non-local patches that are similar to a given patch into a low rank matrix, computing the singular value decomposition of this matrix and minimization of the the nuclear norm of the matrix by soft thresholding with adaptive weights the singular values of this matrix. Even the recently designed methods (for example, [46], which exploits the similarity of patches from external images in addition to the inner patches from the given image, and Deep Learning-based methods such as reported in [11, 45]) produce marginal, if any, improvements compared to WNNM. Nevertheless, some drawbacks common to NSS-based methods are inherent in WNNM. Namely, some over-smoothing effect on the edges and fine texture persists when restoration of severely degraded images.

We propose to combine qWPdn with WNNM algorithms to benefit from the strong features of both algorithms.

Denote by \mathbf{Q} and \mathbf{W} the operators of application of the qWPdn , which is described in Section 2, and WNNM denoising algorithms, respectively, to a degraded array \mathbf{A} : $\mathbf{Q} \mathbf{A} = \mathbf{D}_Q$ and $\mathbf{W} \mathbf{A} = \mathbf{D}_W$.

Assume that we have an array $\check{\mathbf{X}}^0 = \mathbf{X} + \mathbf{E}$, which represents an image \mathbf{X} degraded by additive Gaussian noise \mathbf{E} whose STD is σ . The denoising processing is implemented along the following cross-boosting scheme.

First step: Apply the operators \mathbf{Q} and \mathbf{W} to the input array $\check{\mathbf{X}}^0$: $\mathbf{Y}_Q^1 = \mathbf{Q} \check{\mathbf{X}}^0$ and $\mathbf{Y}_W^1 = \mathbf{W} \check{\mathbf{X}}^0$.

Iterations: $i = 1, \dots, I - 1$

1. Form new input arrays $\check{\mathbf{X}}_Q^i = \frac{\check{\mathbf{X}}^0 + \mathbf{Y}_Q^i}{2}$, $\check{\mathbf{X}}_W^i = \frac{\check{\mathbf{X}}^0 + \mathbf{Y}_W^i}{2}$.
2. Apply the operators \mathbf{Q} and \mathbf{W} to the input arrays: $\mathbf{Y}_Q^{i+1} = \mathbf{Q} \check{\mathbf{X}}_W^i$, $\mathbf{Y}_W^{i+1} = \mathbf{W} \check{\mathbf{X}}_Q^i$.

Estimations of the clean image: Three estimations are used:

1. The cross-boosted WNNM estimation $\tilde{\mathbf{X}}_{uW} \stackrel{\text{def}}{=} \mathbf{Y}_W^I$ (**cbWNNM**).
2. The cross-boosted qWPdn estimation $\tilde{\mathbf{X}}_{uQ} \stackrel{\text{def}}{=} \mathbf{Y}_Q^I$ (**cbqWP**).
3. The hybrid estimation $\tilde{\mathbf{X}}_H \stackrel{\text{def}}{=} (\mathbf{Y}_W^I + \mathbf{Y}_Q^I)/2$ (**hybrid**).



Figure 3.1: Clean images: “Lena”, “Boat”, “Hill”, “Barbara”, “Mandrill”, “Bridge”, “Man”, “Fabric”, “Fingerprint” and “Seismic”

3.3 Experimental results

In this section, we compare the performance of our denoising schemes designated as **cbWNNM** , **cbqWP** and **hybrid** on the restoration of degraded images with the performances of the state-of-the-art algorithms such as BM3D ([15]), BM3D-SAPCA ([16]), WNNM ([22]), NCSR ([18]), cptTP-CTF₆ ([48]) and DAS-2 ([10]). To produce results for the comparison, we used the software available at the websites http://www.cs.tut.fi/~foi/GCF-BM3D/index.html#ref_software (BM3D and BM3D-SAPCA), <http://staffweb1.cityu.edu.hk/xzhuang7/softs/index.html#bdTPCTF> (cptTP-CTF₆ and DAS-2), https://github.com/csjunxu/WNNM_CVPR2014 (WNNM), and <https://www4.comp.polyu.edu.hk/~cslzhang/NCSR.htm> (NCSR).

The restored images were evaluated by the visual perception, by Peak Signal-to-Noise ratio (PSNR) (see Eq. (3.2))⁴ and by the Structural Similarity Index (SSIM) ([43], it is computed by the **ssim.m** Matlab 2020b function). The SSIM measures the structural similarity of small moving windows in two images. It varies from 1 for fully identical windows to -1 for completely dissimilar ones. The global index is the average of local indices. Currently, SSIM is regarded as more informative characteristics of the image quality compared to PSNR and Mean Square Error (MSE) (see discussion in [42]).

For the experiments, we used a standard set of benchmark images: “Lena”, “Boat”, “Hill”, “Barbara”, “Mandrill”, “Bridge”, “Man”, “Fabric” and “Fingerprint”. One image that represents a stacked seismic section is designated as “Seismic”. The ”clean” images are displayed in Fig. 3.1.

The images were corrupted by Gaussian zero-mean noise whose STD was $\sigma = 5, 10, 25, 40, 50, 80$ and 100 dB. Then, the BM3D, BM3D-SAPCA, NCSR, WNNM, cbWNNM , cbqWP, hybrid, cptTP-CTF₆ and DAS-2 denoising algorithms were applied to restore the images. In most experi-

⁴

$$PSNR(\mathbf{x}, \tilde{\mathbf{x}}) \stackrel{\text{def}}{=} 10 \log_{10} \left(\frac{K 255^2}{\sum_{k=1}^K (x_k - \tilde{x}_k)^2} \right) dB. \quad (3.2)$$

ments the algorithm **cbWNNM** performed better than **cbqWP**. However, this was not the case in experiments with the “Seismic” image. Therefore, in the “Seismic” block in Table 3.2 and pictures in Fig. 3.7 we provide results from experiments with the **cbqWP** rather than with the **cbWNNM** algorithm.

Table 3.1 summarizes experimental results from the restoration of the “Barbara”, “Boat”, “Fingerprint”, “Lena” and “Mandrill” images corrupted by additive Gaussian noise. PSNR and SSIM values for each experiment are given.

Table 3.2 summarizes experimental results from the restoration of the “Hill”, “Seismic”, “Fabric”, “Bridge” and “Man” images corrupted by additive Gaussian noise. The PSNR and SSIM values for each experiment are given.

Table 3.3 provides the PSNR and SSIM values from Tables 3.1 and 3.2, which are averaged over ten images participating in the experiments. Respective diagrams are drawn in Fig. 1.1.

It is seen from Tables 3.1, 3.2 and 3.3 that our methods **cbWNNM** and **hybrid** produce PSNR values very close to (sometimes higher than) those produced by the WNNM and BM3D-SAPCA methods and higher than those from BM3D, NCSR, cptTP- \mathcal{CTF}_6 and DAS-2 denoising algorithms. On the other hand, the SSIM values for the images restored by **cbWNNM** and **hybrid** significantly exceed the SSIM values from all other methods. Especially it is true for the restoration of images in presence of a strong noise. This observation reflects the fact that directional qWPs have exceptional capabilities to capture fine structures even in severely degraded images. This fact is illustrated by Figures 3.2, 3.3, 3.4, 3.5, 3.6 and 3.7, which display results of restoration of several images corrupted by strong Gaussian noise. In all those cases the SSIM values from the **cbWNNM** and **hybrid** algorithms significantly exceed values from all other algorithms. Respectively, the restoration of the images’ fine structure by the **cbWNNM** and **hybrid** algorithms is much better compared to the restoration by other algorithms.

Each of the mentioned figures comprises 12 frames, which are arranged in a 4×3 order:

$$\begin{pmatrix} f_{11} & f_{12} & f_{13} \\ f_{21} & f_{22} & f_{23} \\ f_{31} & f_{32} & f_{33} \\ f_{41} & f_{42} & f_{43} \end{pmatrix}.$$

Here frame f_{11} displays noised image; frame f_{21} – image restored by BM3D; f_{12} – image restored by BM3D-SAPCA; f_{22} – image restored by WNNM; f_{13} – image restored by **cbWNNM**⁵; f_{23} – image restored by **hybrid**. Frame f_{31} displays a fragment of the original image. The remaining frames $\{f_{32}, f_{33}, f_{41}, f_{42}, f_{43}\}$ display the fragments of the restored images shown in frames $\{f_{12}, f_{13}, f_{21}, f_{22}, f_{23}\}$, which are arranged in the same order.

3.4 Relation of the proposed algorithms to the Deep Learning methods

In recent years, the focus of the image denoising research shifted to the Deep Learning methods, which resulted in a huge amount of publications. We mention a few of them: [11, 45, 13, 19, 39, 32, 35, 40]. Much more references can be found in the reviews [41, 26]. One of advantages of the Deep Learning methods is that, once the Neural Net is trained (which can involve extended datasets and take several days), its application to test images is very fast. Therefore, the experimental results in most related publications are presented via the PSNR and, sometimes, the SSIM values averaged over some test datasets such as, for example, Set12 introduced in [45].

Set12 partially overlap with the set of 10 (Set10) images that we used in our experiments.

⁵For the “Seismic” image **cbqWP** instead of **cbWNNM**.

Table 3.1: PSNR/SSIM values from restoration of “Barbara”, “Boat”, “Fingerprint”, “Lena” and “Mandrill” images. Boldface highlights the best results. Noise $STD=\sigma$

σ	5	10	25	40	50	80	100
Barbara							
noised	34.16/0.77	28.14/0.6	20.18/0.35	16.09/0.23	14.16/0.18	10.07/0.09	8.14/0.06
WNNM	38.77 /0.836	35.51 /0.7733	31.27 /0.68	28.77/0.5993	27.8/0.5628	25.48/0.4499	24.36/0.3891
SAPCA	38.37/0.8445	35.1/0.7756	31/0.6797	28.68/0.6086	27.5/0.5605	24.3/0.402	23.09/0.339
NCSR	38.37/0.8302	35.4/0.7674	30.62/0.6579	28.19/0.5687	27/0.5176	24.37/0.3902	23.21/0.3296
cptTP-CTF ₆	37.71/0.8382	34.04/0.763	29.24/0.6358	26.75/0.5375	25.61/0.4833	23.44/0.3633	22.55/0.3092
DAS-2	37.7/0.8438	33.98/0.764	29.4/0.6422	27.09/0.5595	26.01/0.5121	23.72/0.3987	22.63/0.3398
BM3D	38.3/0.8387	34.97/0.7738	30.71/0.6707	27.98/0.5788	27.23/0.5389	24.79/0.4192	23.63/0.3608
cbWNNM	38.74/0.853	35.4/0.7833	31.11/ 0.6852	28.9/0.6171	27.81/0.576	25.51 /0.4681	24.47 /0.4076
Hybrid	38.59/ 0.8543	35.25/ 0.7859	30.87/0.6834	28.67/0.6154	27.59/0.5745	25.35/ 0.4688	24.33/ 0.4114
Boat							
noised	34.16/0.79	28.14/0.58	20.18/0.29	16.09/0.18	14.16/0.13	10.07/0.07	8.14/0.05
WNNM	37.35/0.8042	34.07/0.6803	30.05 /0.5266	27.96 /0.4317	26.98/0.3833	25.03/0.2853	24.11/0.2389
SAPCA	37.51 / 0.8288	34.1 /0.6925	30.03/0.5282	27.92/0.4384	26.89/0.3931	24.68/0.2993	23.69/0.2609
NCSR	37.33/0.8101	33.92/0.6848	29.78/0.5053	27.64/0.4003	26.4/0.3551	24.61/0.257	23.69/0.217
cptTP-CTF ₆	36.86/0.8044	33.34/0.6713	29.12/0.504	27.02/0.4044	26.09/0.3567	24.27/0.2626	23.48/0.2232
DAS-2	36.85/0.8294	33.15/0.688	28.88/0.5182	26.78/0.4228	25.81/0.3763	23.84/0.2792	22.9/0.2361
BM3D	37.29/0.8065	33.91/0.6805	29.9/0.5296	27.74/0.4395	26.77/0.3899	24.87/0.2952	23.96/0.2533
cbWNNM	37.42/0.8257	34.03/0.702	29.99/0.5455	27.95/0.4568	27 /0.4113	25.09 /0.3116	24.26 /0.2638
Hybrid	37.13/0.8194	33.86/ 0.7105	29.72/0.5521	27.66/0.4616	26.78/0.4158	24.92/0.3182	24.14/0.2725
Fingerprint							
noised	34.16/0.97	28.14/0.91	20.18/0.67	16.09/0.48	14.16/0.38	10.07/0.21	8.14/0.15
WNNM	35.16/0.9801	32.68/ 0.9655	27.94 /0.9014	25.6/0.8388	24.7 /0.8093	22.77/0.7289	21.85/0.6777
SAPCA	36.66/0.9859	32.64/0.9648	27.8/0.8981	25.54/0.839	24.53/0.8057	22.3/0.7068	21.18/0.6449
NCSR	36.8/0.9860	32.69 /0.9645	27.83/0.8968	25.52/0.8290	24.48/0.7894	22.37/0.6869	21.4/0.6295
cptTP-CTF ₆	36/0.9845	32.23/0.9619	27.33/0.889	25.07/0.8219	24.04/0.7815	21.98/0.6746	21.03/0.6129
DAS-2	36.25/0.9843	32.03/0.9601	27.07/0.886	24.86/0.8246	23.88/0.7895	21.87/0.7013	20.96/0.652
BM3D	36.5/0.9854	32.45/0.9634	27.71/0.8955	25.3/0.8334	24.53/0.8019	22.2/0.7165	21.61/0.6643
cbWNNM	36.91 / 0.9864	32.1/0.9615	27.85/0.9039	25.68 /0.851	24.67/0.8215	22.79 /0.7417	21.89 /0.7031
Hybrid	36.8/0.9861	32.51/0.9645	27.88/ 0.904	25.63/0.8512	24.59/0.8213	22.73/0.7425	21.77/0.7061
Lena							
noised	34.16/0.65	28.14/0.43	20.18/0.2	16.09/0.12	14.16/0.09	10.07/0.04	8.14/0.03
WNNM	38.8 /0.7131	36.05/0.6193	32.25 /0.5036	30.1/0.425	29.24/0.3942	27.22/0.3208	26.19/0.278
SAPCA	38.67/0.6893	36.07 /0.6233	32.23/0.5077	30.11/0.4411	29.07/0.408	26.5/0.314	25.1/0.2771
NCSR	38.73/0.7123	35.85/0.6214	31.92/0.4841	29.91/0.4155	28.9/0.382	26.72/0.3025	25.71/0.2685
cptTP-CTF ₆	38/0.705	35.46/0.616	31.53/0.4992	29.41/0.4313	28.41/0.3965	26.36/0.3199	25.41/0.2833
DAS-2	38.18/0.7272	35.2/0.625	31.09/0.4920	28.9/0.4148	27.84/0.3757	25.53/0.29	24.4/0.2285
BM3D	38.72/0.7078	35.92/0.6233	32.07/0.5026	29.87/0.4265	29.04/0.3957	26.98/0.3214	25.95/0.2851
cbWNNM	38.79/0.7095	36/0.633	32.20/0.5155	30.2 /0.4479	29.25 /0.4139	27.24 / 0.3359	26.36 /0.304
Hybrid	38.76/ 0.7218	35.89/ 0.6408	32.02/ 0.5202	30/0.4528	29.06/ 0.4193	27.07/0.3349	26.21/ 0.312
Mandrill							
noised	34.16/0.7	28.14/0.52	20.18/0.51	16.09/0.34	14.16/0.26	10.07/0.14	8.14/0.1
WNNM	34.7/0.8902	30.36/0.7994	25.44/0.605	23.43 /0.4739	22.58 /0.4024	21.1 /0.2645	20.46 /0.1949
SAPCA	35.2 /0.9281	30.59 /0.8278	25.54 /0.6244	23.4/0.4843	22.54/0.413	20.92/0.2649	20.3/0.2048
NCSR	35.07/0.9129	30.38/0.7986	25.36/0.5908	23.18/0.4325	22.35/0.3669	20.82/0.2215	20.23/0.162
cptTP-CTF ₆	35.06/0.9252	30.32/0.8198	25.3/0.6082	23.16/0.4531	22.25/0.371	20.72/0.2148	20.2/0.1617
DAS-2	35.02/ 0.9301	30.24/0.8329	25.24/0.64	23.2/0.51	22.34/0.4423	20.8/0.2997	20.14/0.2376
BM3D	34.98/0.9209	30.34/0.8135	25.27/0.6095	23/0.4613	22.27/0.3813	20.9/0.2439	20.39/0.1956
cbWNNM	34.34/0.9158	30.39/ 0.8359	25.53 / 0.6631	23.35 / 0.5477	22.39/0.4802	20.68/0.3513	20.03/0.2841
Hybrid	33.23/0.9028	30.02/0.8303	25.4/0.6625	1723.14/0.5471	22.28/ 0.4887	20.31/ 0.3565	19.59/ 0.2945

Table 3.2: PSNR/SSIM values from restoration of “Hill”, “Seismic”, “Fabric”, “Bridge” and “Man” images. Boldface highlights the best results. Noise STD= σ .

σ	5	10	25	40	50	80	100
Hill							
noised	34.16/0.8	28.14/0.59	20.18/0.27	16.09/0.15	14.16/0.11	10.07/0.05	8.14/0.03
WNNM	37.02/0.8239	33.7/0.7121	29.96/0.5225	28.18 /0.4203	27.34/0.373	25.63/0.2822	24.75/0.236
SAPCA	37.3 /0.8457	33.84 /0.7316	29.95/0.5335	28.09/0.4281	27.2/0.3815	25.18/0.2867	24.29/0.2491
NCSR	37.17/0.8350	33.7/0.7246	29.72/0.5138	27.84/0.3936	26.99/0.3463	25.16/0.2480	24.35/0.2089
cptTP-CTF ₆	36.83/0.8388	33.17/0.7157	29.13/0.4992	27.37/0.3903	26.59/0.3425	25/0.2495	24.29/0.2108
DAS-2	36.68/0.8447	33.02/0.7292	29.15/0.5327	27.31/0.4245	26.47/0.3747	24.62/0.2733	23.7/0.2272
BM3D	37.14/0.8384	33.61/0.7193	29.85/0.5311	27.99/0.4305	27.19/0.3825	25.42/0.2878	24.59/0.2448
cbWNNM	37.2/0.8515	33.72/0.7461	30.01 /0.5545	28.13/0.4584	27.4 /0.4033	25.64 /0.3148	24.87 /0.2718
Hybrid	37.09/ 0.8516	33.64/ 0.7511	29.86/ 0.5655	28.01/0.4642	27.29/0.4118	25.62/0.3215	24.84/ 0.278
Seismic							
noised	34.16/0.8	28.14/0.55	20.18/0.22	16.09/0.12	14.16/0.08	10.07/0.04	8.14/0.03
WNNM	39.26/0.9205	34.95/0.765	30.65/0.4556	28.93/0.3092	28.34/0.2524	27.11 /0.1621	26.56 /0.1305
SAPCA	39.09/0.9167	35.04/0.7871	30.8/0.5016	29.04/0.3654	28.2/0.3124	26.34/0.23	25.4/0.1934
NCSR	38.97/0.9131	34.86/0.78	30.62/0.4643	29/0.2948	28.27/0.2374	26.81/0.139	26.25/0.1089
cptTP-CTF ₆	38.81/0.9107	34.83/0.7696	30.72/0.4616	29.1/0.3188	28.4/0.2618	26.91/0.1616	26.16/0.127
DAS-2	38.8/0.9141	34.83/0.795	30.67/0.5383	28.87/0.3938	28.05/0.3318	26.22/0.2222	25.29/0.1785
BM3D	39/0.9126	34.9/0.77	30.8/0.4984	29.08/0.3606	28.45 /0.2853	26.97/0.19	26.31/0.1547
cbqWP	39.57/0.9318	35.41/0.8321	30.89/ 0.5849	28.98/ 0.445	27.97/ 0.3836	25.42/ 0.2755	23.36/ 0.2299
Hybrid	39.13/0.9241	35.41/0.8266	30.99 /0.5745	29.26 /0.4298	28.4/0.369	26.28/0.2657	24.75/0.2227
Fabric							
noised	34.16/0.8	28.14/0.55	20.18/0.22	16.09/0.12	14.16/0.08	10.07/0.04	8.14/0.03
WNNM	38.75 /0.833	34.92/0.7318	30.76/0.5488	28.83/0.4485	28.01 /0.4113	26.19 /0.3361	25.26 /0.2992
SAPCA	38.72/0.8351	35/0.7432	30.8/0.5678	28.82/ 0.4726	27.89/0.3905	25.54/0.3275	24.51/0.2915
NCSR	38.58/0.8263	34.78/0.7298	30.53/0.5408	28.54/0.4384	27.69/0.3988	25.77/0.3185	24.8/0.2838
cptTP-CTF ₆	37.99/0.81	34.07/0.6978	29.73/0.5127	27.83/0.4266	26.94/0.3905	25.12/0.3185	24.23/0.2856
DAS-2	37.74/0.8017	33.78/0.6985	29.48/0.5223	27.48/0.4283	26.52/0.3858	24.45/0.3017	23.42/0.2641
BM3D	38.47/0.8303	34.63/0.7262	30.57/0.5476	28.65/0.4548	27.85/0.4182	26/0.3402	25.06/0.3032
cbWNNM	38.69/ 0.8354	34.92/0.7426	30.74/0.5649	28.84/0.4726	27.96/0.4279	26.15/0.3489	25.26/0.3128
Hybrid	38.52/0.8294	34.76/0.7349	30.52/0.561	28.61/0.4718	27.73/ 0.4283	25.9/ 0.352	25.01/0.3096
Bridge							
noised	34.16/0.7	28.14/0.52	20.18/0.51	16.09/0.34	14.16/0.26	10.07/0.14	8.14/0.1
WNNM	35.81/0.9387	31.17/0.854	26.29/0.635	24.45/0.4992	23.67/0.43	22.24 /0.3095	21.6/0.2568
SAPCA	35.89/0.9439	31.35 /0.8671	26.44/0.6587	24.5 /0.5152	23.7 /0.4465	22.17/0.3273	21.48/0.2783
NCSR	35.78/0.9375	31.2/0.8551	26.29/0.6389	24.31/0.4814	23.54/0.4169	22.02/0.2832	21.36/0.2344
cptTP-CTF ₆	35.56/0.9388	30.94/0.8575	26/0.6362	24.01/0.4803	23.22/0.4067	21.78/0.2744	21.17/0.2263
DAS-2	35.44/0.9373	30.76/0.8573	25.91/0.6609	24.03/0.5287	23.22/0.4625	21.66/0.3316	20.94/0.2768
BM3D	35.78/0.9415	31.17/0.8597	26.22/0.641	24.3/0.5007	23.58/0.4286	22.22/0.3168	21.61 /0.2716
cbWNNM	35.77/0.9412	31.28/ 0.869	26.45 /0.6838	24.49/0.5587	23.68/0.4963	22.05/0.3717	21.37/0.3158
Hybrid	35.45/0.9362	31.12/0.8643	26.23/ 0.684	24.24/ 0.5659	23.32/ 0.5033	21.57/ 0.3822	20.77/ 0.3292
Man							
noised	34.16/0.75	28.14/0.55	20.18/0.27	16.09/0.16	14.16/0.12	10.07/0.06	8.14/0.04
WNNM	37.99/0.8267	34.19/0.7234	29.79/0.5403	27.8/0.4326	26.95/0.3842	25.18 /0.2911	24.34 /0.2455
SAPCA	38.09 /0.8387	34.28 /0.7325	29.84 /0.5488	27.86 /0.445	26.97 /0.3997	24.92/0.3078	23.9/0.2677
NCSR	37.88/0.8216	34.08/0.7212	29.62/0.5289	27.58/0.4107	26.7/0.3632	24.89/0.2671	24.05/0.2276
cptTP-CTF ₆	37.44/0.8302	33.59/0.7235	29.14/0.5341	27.14/0.4241	26.25/0.3725	23.99/0.2713	23.73/0.229
DAS-2	37.1/0.7525	33.16/0.7184	28.81/0.5374	26.84/0.4326	25.93/0.3815	23.99/0.2783	23.06/0.2336
BM3D	37.85/0.8306	34.02/0.7225	29.65/0.5429	27.68/0.442	26.84/0.3919	25.09/0.3009	22.26/0.2598
cbWNNM	37.97/0.8422	34.19/0.7428	29.81/0.5646	27.81/0.4622	26.82/0.4173	25.04/0.3216	24.11/0.2806
Hybrid	37.75/ 0.8426	34.02/ 0.7452	29.65/ 0.5674	27.61/ 0.4664	26.63/ 0.4195	24.84/ 0.3257	23.88/ 0.285



Figure 3.2: Restoration of the “Hill” image corrupted by Gaussian noise with $\text{STD } \sigma = 50 \text{ dB}$.
PSNR/SSIM for BM3D– 27.19/0.3825; for WNNM– 27.34/0.373; for BM3D-SAPCA–27.2/0.3815; for **cbWNNM**–27.4/0.4033; for **hybrid**–27.29/0.4118



Figure 3.3: Restoration of “Barbara” image corrupted by Gaussian noise with $\text{STD } \sigma = 80 \text{ dB}$.
PSNR/SSIM for BM3D– 24.79/0.4192; for WNNM– 25.48/0.4499; for BM3D-SAPCA–24.33/0.402;
for **cbWMNN**–25.51/0.4681; for **hybrid**–25.35/0.4688

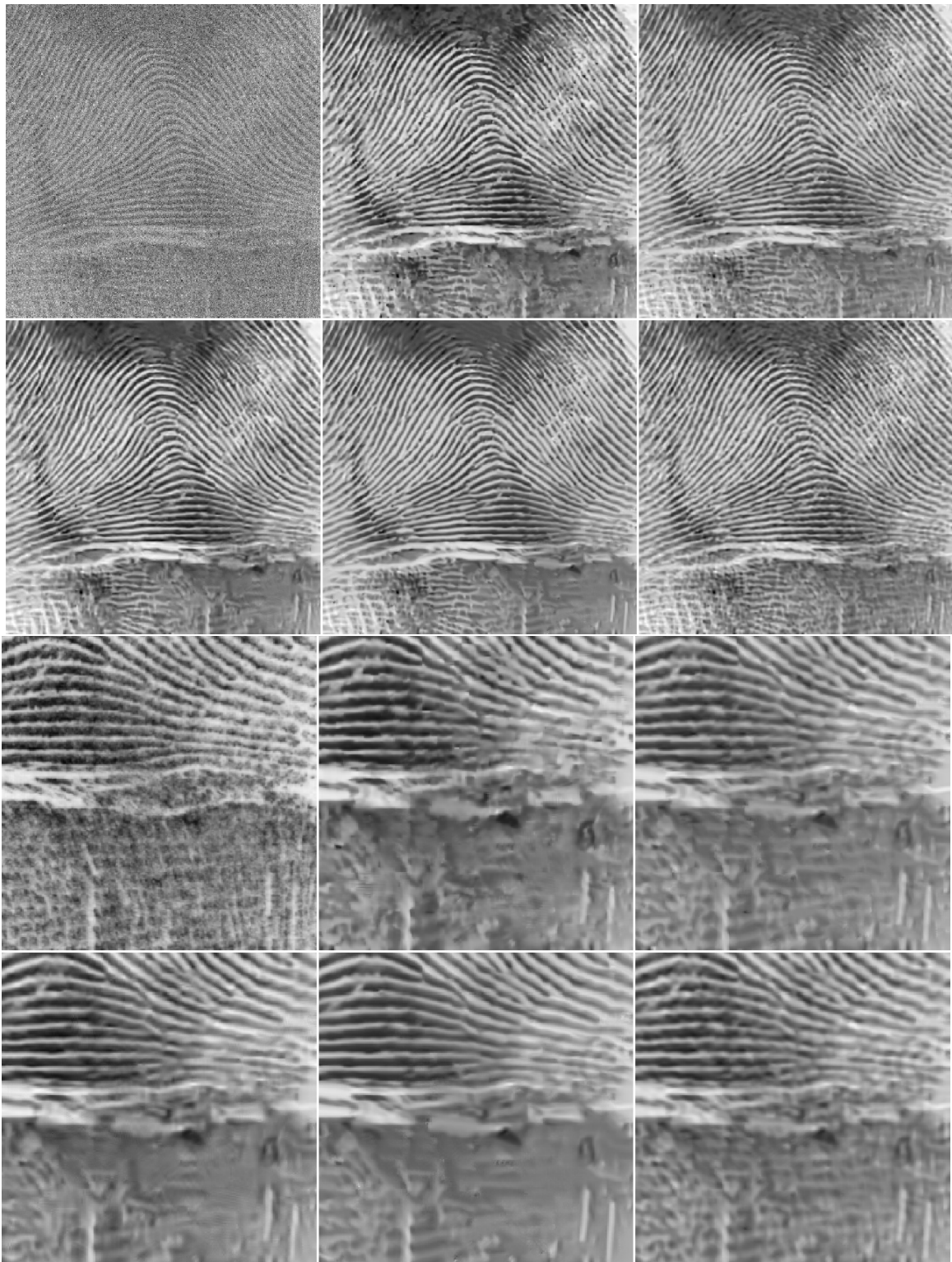


Figure 3.4: Restoration of “Fingerprint” image corrupted by Gaussian noise with $\text{STD } \sigma = 80 \text{ dB}$.
PSNR/SSIM for BM3D– 22.2/0.7165; for WNNM– 22.77/0.7289; for BM3D-SAPCA–22.3/0.7068;
for upWMMN–22.79/0.7417; for hybrid–22.73/0.7425

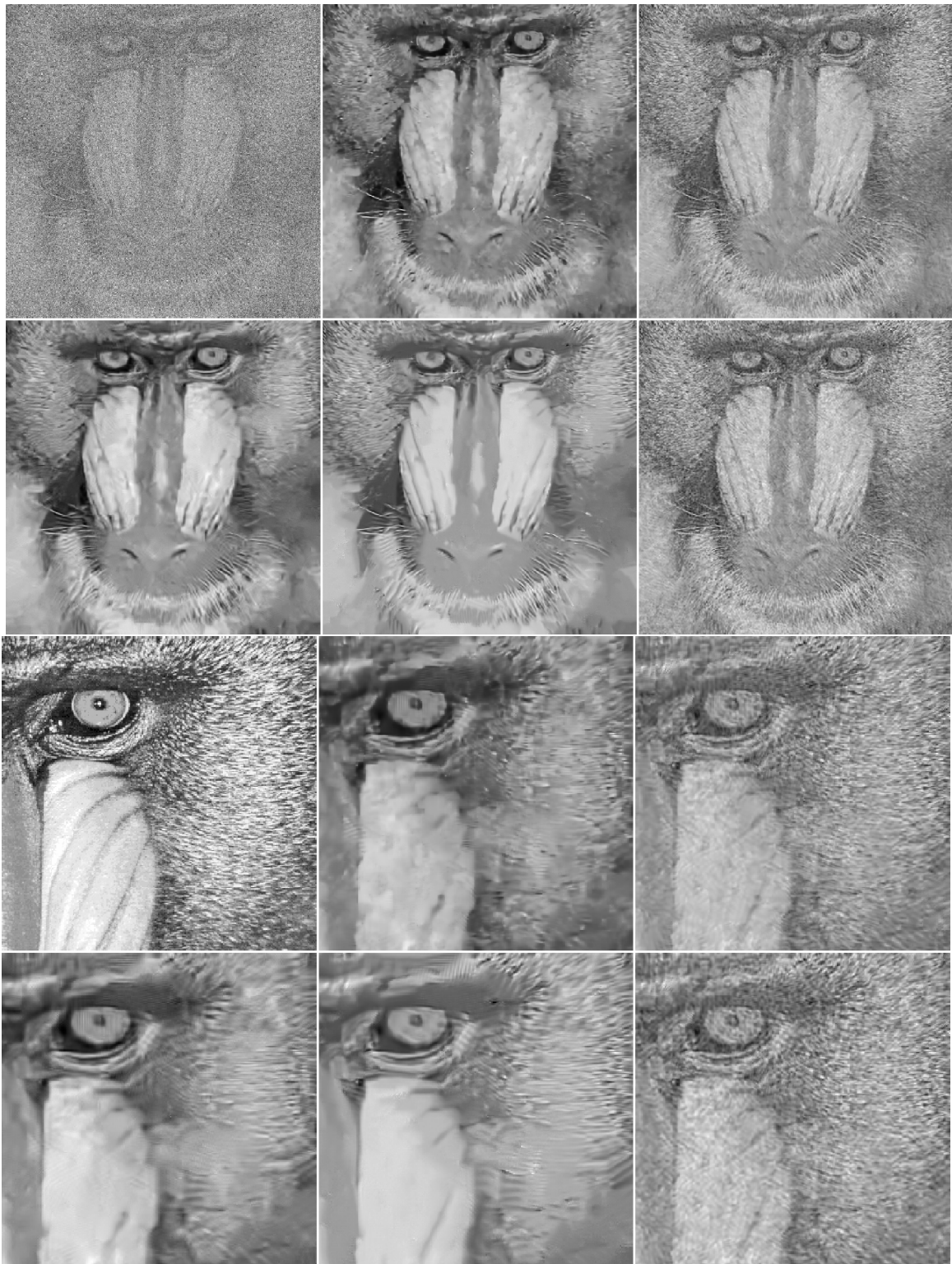


Figure 3.5: Restoration of “Mandrill” image corrupted by Gaussian noise with $\text{STD } \sigma = 80 \text{ dB}$.
PSNR/SSIM for BM3D– 20.9/0.2439; for WNNM– 21.1/0.2645; for BM3D-SAPCA–20.92/0.2649;
for **cbWNNM**–20.68/0.3513; for **hybrid**–20.31/0.3565



Figure 3.6: Restoration of “Bridge” image corrupted by Gaussian noise with $\text{STD } \sigma = 40 \text{ dB}$.
PSNR/SSIM for BM3D- 24.3/0.5007; for WNNM- 24.45/0.4992; for BM3D-SAPCA-24.5/0.5152;
for **cbWNNM**-24.49/0.5587; for **hybrid**-24.24/0.5659

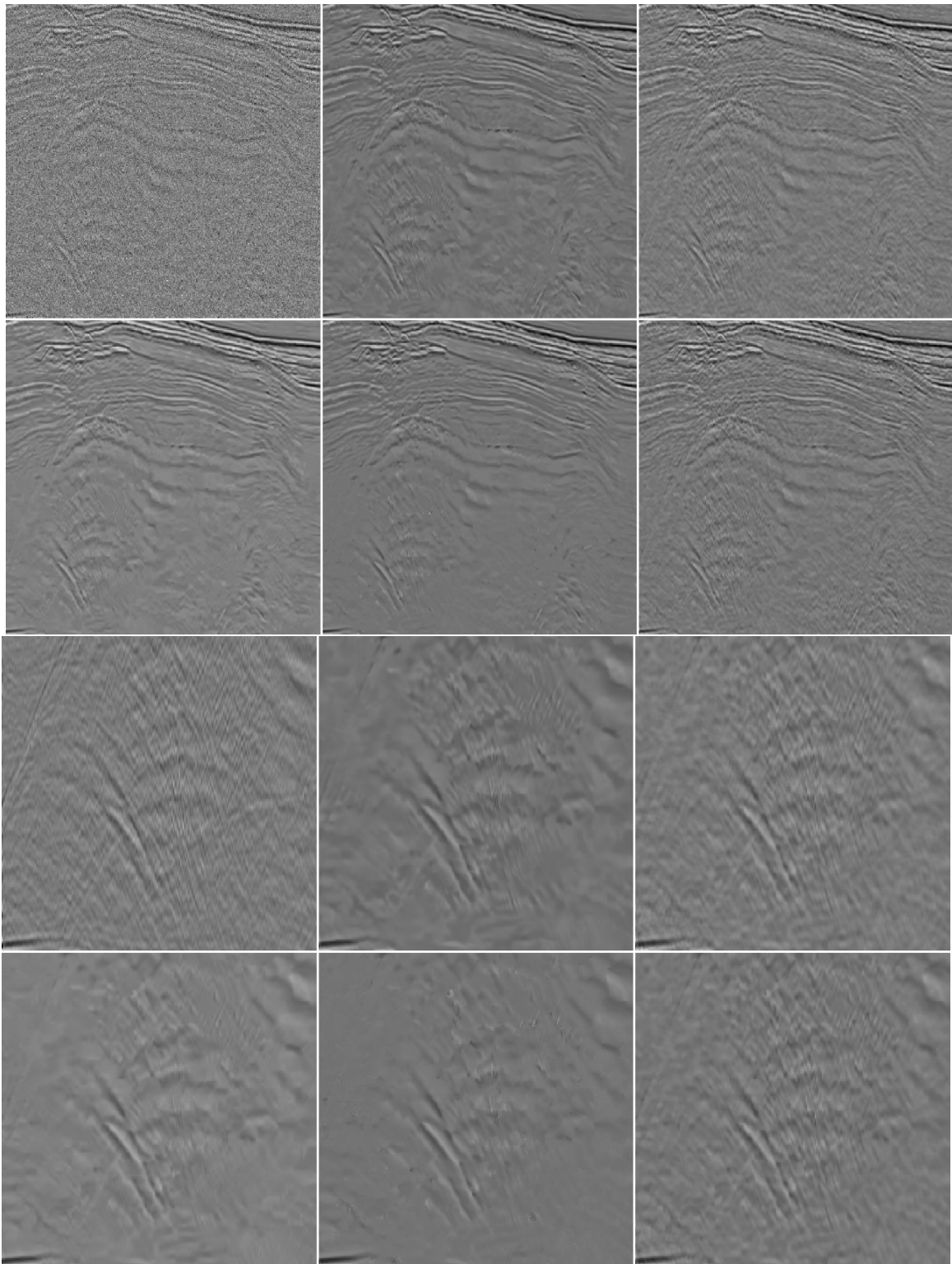


Figure 3.7: Restoration of “Seismic” image corrupted by Gaussian noise with $\text{STD } \sigma = 25 \text{ dB}$.
PSNR/SSIM for BM3D–30.8/0.4984; for WNNM–30.65/0.4556; for BM3D-SAPCA–30.8/0.5016;
for **cbqWP**–30.89/0.5849; for **hybrid**–30.99/0.5745

Table 3.3: PSNR/SSIM values averaged over 10 images. Boldface highlights the highest values. Noise $STD=\sigma$.

σ	5	10	25	40	50	80	100
WNNM	37.63 /0.8649	33.81 /0.768	29.46 /0.5949	27.34/0.489	26.56 /0.4405	24.8 /0.3405	23.95 /0.2916
SAPCA	37.57/0.8685	33.8/0.7745	29.44/0.6048	27.4/0.5038	26.45/0.4511	24.29/0.3466	23.29/0.3
NCSR	37.44/0.8586	33.65/0.765	29.2/0.5819	27.13/0.4664	26.2/0.4163	24.33/0.3105	23.48/0.2662
cptTP-CTF ₆	37.03/0.8586	33.2/0.7596	28.72/0.578	26.69/0.4688	25.78/0.4163	23.96/0.311	23.23/0.2669
DAS-2	36.98/0.8565	33.02/0.7668	28.56/0.597	26.54/0.494	25.61/0.4432	23.67/0.3376	22.74/0.2874
BM3D	37.4/0.8613	33.59/0.7652	29.28/0.5969	27.15/0.4928	26.36/0.4414	24.54/0.3432	23.54/0.2993
cbWNNM	37.54 / 0.8692	33.74/0.7848	29.46 /0.6266	27.43 /0.5317	26.5/0.4831	24.56/0.3841	23.6/0.3373
Hybrid	37.25/0.8668	33.65/ 0.7854	29.31/ 0.6275	27.28/ 0.5326	26.37/ 0.4852	24.46/ 0.3868	23.53/ 0.3421

Table 3.4: P_{method}/S_{method} , where the PSNR and SSIM values are averaged over either Set12 or Set10. Noise $STD=\sigma$.

σ	10	15	25	50	70	80	100
Cola_Net	-	1.028/1.016	1.031/1.025	1.04/1.046	1.041/1.06	-	-
CDNet	-	1.019/1.016	1.016/1.01	1.025/1.074	1.027/1.057	1.027/1.065	-
FLCNN	-	1.022/1.02	1.017/1.011	1.028/1.039	-	-	-
DRCNN	-	1.016/1.036	1.02/1.033	1.02/1.039	-	-	-
SRENSS	1.044/1.011	-	-	1.02/1.028	1.011/1.028	-	1.006/1.0038
WNNM	1.007/1.004	-	1.006/0.997	1.007/0.998	-	1.01/0.992	1.018/0.974
hybrid	1.002/1.026	-	1.008/1.051	1.001/1.099	-	0.997/1.127	0.999/1.143

Namely the images “Barbara”, “Boat”, “Fingerprint”, “Hill”, “Lena” and “Man” participate in both sets. The structure of the remaining images “Seismic”, “Fabric”, “Mandrill” and “Bridge” from Set10 is more complicated compared to the images “Camera”, “Couple”, “House”, “Monarch”, “Pepper” and “Straw” from Set12. Therefore, the averaged results comparison from these two datasets is quite justified. For even better compatibility, we compare the gains of results from different methods over the corresponding results from BM3D: $P_{method} \stackrel{\text{def}}{=} \frac{PSNR_{method}}{PSNR_{BM3D}}$ and $S_{method} \stackrel{\text{def}}{=} \frac{SSIM_{method}}{SSIM_{BM3D}}$. Recall that for the calculation of SSIM we use the function `ssim` from Matlab 2020b, whereas in most publications SSIM is computed by some other schemes.

We compare results from the recent state-of-the-art algorithms Cola_Net ([34], (2022)), CDNet ([35], (2021)), FLCNN ([40], (2021)), DRCNN ([32], (2020)), and the non-Deep Learning algorithm presented in [46] (2021), which we mark as SRENSS, averaged over Set12 with the results from WNNM [22] and the proposed **hybrid** algorithm averaged over Set10⁶. The PSNR and SSIM values for all methods except for WNNM and **hybrid** are taken from the corresponding publications. Table 3.4 shows the results of this comparison.

We can observe from the table that all participated up-to-date schemes, including the non-Deep Learning algorithm SRENSS, demonstrate a moderate gain over BM3D in both PSNR and SSIM values averaged over Set12 (far from being a breakthrough). The values from WNNM averaged over Set10 are very close to those from BM3D averaged over the same set. The same can be said for the PSNR values from the **hybrid** algorithm. However, the SSIM values from the **hybrid** algorithm demonstrate a strong gain over BM3D, which is clearly seen in Fig. 1.1 and Table 3.3. Especially

⁶Averaged results from **upBM3D** are almost identical to those from **hybrid** algorithm.

it is true for a strong Gaussian noise with $\sigma = 80, 100$ dB. This fact highlights the ability of the qWP-based algorithms to restore edges and fine structures even in severely damaged images.

Note that denoising results presented in the overwhelming majority of the Deep Learning publications deal with the noise level not exceeding 50 dB.

4 Discussion

We presented a denoising scheme that combines the qWPdn algorithm based on the directional quasi-analytic wavelet packets, which are designed in [3], with the state-of-the-art denoising algorithm WNNM ([22]) considered to be one of the best in the field. Either of the two algorithms has their strong features and shortcomings. The qWPdn algorithm described in Section 3.1 demonstrates the ability to restore edges and texture details even from severely degraded images. This ability stems from the fact that the designed 2D qWP transforms provide a variety of 2D testing waveforms, which are close to windowed cosine waves with multiple frequencies oriented in multiple directions. In most separate experiments, the qWPdn method demonstrated better resolution of edges and fine structures compared to the WNNM algorithm, which were reflected by the higher SSIM values. In turn, the WNNM algorithm is superior for noise suppression, especially in smooth regions in images, thus producing the highest PSNR values in almost all the experiments. However, some over-smoothing effect on the edges and fine texture persisted with the WNNM algorithm when noise was strong.

The qWPdn and WNNM methods complement each other. Therefore, the idea to combine these methods is natural. In the iterative hybrid scheme qWPdn–WNNM, which is proposed in Section 3.2, the output from one algorithm updates the input to the other. Such a hybrid method has some distant relation to the SOS boosting scheme presented in [36]. The main distinction between the qWPdn–WNNM and the SOS boosting is that each of the qWPdn and WNNM algorithms is “boosted” by the output from the other algorithm. Such a scheme can be regarded as a *Cross-Boosting*.

The scheme proved to be highly efficient. It is confirmed by a series of experiments on restoration of 10 multimedia images of various structure, which were degraded by Gaussian noise of various intensity. In the experiments, the performance of two combined qWPdn–WNNM algorithms was compared with the performance of six advanced denoising algorithms BM3D, BM3D-SAPCA ([16]), WNNM ([22]), NCSR ([18]), cptTP-CTF₆ ([48]) and DAS-2 ([10]). In almost all the experiments reported in Section 3.3, the two combined algorithms produce PSNR values, which are very close to the values produced by WNNM and BM3D-SAPCA. Their noise suppression efficiency is competitive with that of WNNM and BM3D-SAPCA. On the other hand, their results in the resolution of edges and fine structures are much better than the results from all other algorithms participating in the experiments. This is seen in the images presented in Section 3.3. Consequently, the SSIM values produced by the cross-boosted algorithms qWPdn–WNNM are significantly higher than the values produced by all other participated algorithms.

Disscussion in Section 3.4 shows that the qWPdn–WNNM algorithms can, in some aspects, compete with the Deep Learning denoising methods.

Acknowledgment This research was partially supported by the Israel Science Foundation (ISF, 1556/17), Blavatnik Computer Science Research Fund Israel Ministry of Science and Technology 3-13601 and 3-14481.

References

- [1] A. Averbuch, R. R. Coifman, D. L. Donoho, M. Israeli, and Y. Shkolnisky. A framework for discrete integral transformations I – the pseudopolar Fourier transform. *SIAM Journal on Scientific Computing*, 30(2):764–784, 2008.
- [2] A. Averbuch, R. R. Coifman, D. L. Donoho, M. Israeli, Y. Shkolnisky, and I. Sedelnikov. A framework for discrete integral transformations II – the 2d discrete Radon transform. *SIAM Journal on Scientific Computing*, 30(2):785–803, 2008.
- [3] A. Averbuch, P. Neittaanmäki, and V. Zheludev. Directional wavelet packets originating from polynomial splines. <http://arxiv.org/abs/2008.05364>.
- [4] A. Averbuch, P. Neittaanmäki, and V. Zheludev. *Splines and spline wavelet methods with application to signal and image processing, Volume III: Selected topics*. Springer, 2019.
- [5] A. Averbuch, P. Neittaanmäki, V. Zheludev, M. Salhov, and J. Hauser. Image inpainting using directional wavelet packets originating from polynomial splines. *Signal Processing: Image Communication*, 97, 2021. <http://arxiv.org/abs/2001.04899>.
- [6] I. Bayram and I. W. Selesnick. On the dual-tree complex wavelet packet and m-band transforms. *IEEE Trans. Signal Process.*, 56:2298–2310, 2008.
- [7] A. Buades, B. Coll, and J.-M. Morel. A review of image denoising algorithms, with a new one. *Multiscale Model. Simul.*, 4(2):490–530, 2005.
- [8] E. Candés, L. Demanet, D. Donoho, and L. X. Ying. Fast discrete curvelet transforms. *Multiscale Model. Simul.*, 5:861–899, 2006.
- [9] E. Candés and D. Donoho. New tight frames of curvelets and optimal representations of objects with piecewise c^2 singularities. *Commun. Pure Appl. Math.*, 57:219–266, 2004.
- [10] Z. Che and X. Zhuang. Digital affine shear filter banks with 2-layer structure and their applications in image processing. *IEEE Trans. on Image Processing*, 27(8):3931–3941, 2018.
- [11] Y. Chen and T. Pock. Trainable nonlinear reaction diffusion: a flexible framework for fast and effective image restoration. *IEEE Trans. on Pattern analysis and Machine Intelligence*, 39(6):1256–1272, 2017.
- [12] R. R. Coifman and V. M. Wickerhauser. Entropy-based algorithms for best basis selection. *IEEE Trans. Inform. Theory*, 38(2):713–718, 1992.
- [13] Cristóvão Cruz, Alessandro Foi, Vladimir Katkovnik, and Karen Egiazarian. Nonlocality-reinforced convolutional neural networks for image denoising. *IEEE Signal Processing Letters*, 25(8):1216–1220, 2018.
- [14] L. Šendur and I. W. Selesnick. Bivariate shrinkage functions for wavelet-based denoising exploiting interscale dependency. *IEEE Trans. Signal Process.*, 50:2744–2756, 2002.
- [15] K. Dabov, A. Foi, V. Katkovnik, and K. Egiazarian. Image denoising by sparse 3d transform-domain collaborative filtering. *IEEE Trans. Image Process.*, 16(8):2080—2095, 2007.

- [16] K. Dabov, A. Foi, V. Katkovnik, and K.O. Egiazarian. BM3D image denoising with shape adaptive principal component analysis. In *Proceedings of the Workshop on Signal Processing with Adaptive Sparse Structured Representations (SPARS'09)*, 2009.
- [17] M. N. Do and M. Vetterli. Contourlets. In *Beyond Wavelets, G. V. Welland, ed.* Academic Press, San Diego, CA, 2008.
- [18] W.S. Dong, L. Zhang, G.M. Shi, and X. Li. Nonlocally centralized sparse representation for image restoration. *IEEE Trans. Image Process.*, 22(4):1620–1630, 2013.
- [19] Y. Fang and T. Zeng. Learning deep edge prior for image denoising. *Computer Vision and Image Understanding*, 200:103044, 2020.
- [20] W.-Q Lim G. Kutyniok and X. Zhuang. Digital shearlet transforms. In *Shearlets: Multiscale Analysis for Multivariate Data*, pages 239–282. Birkhäuser, Boston, 2012.
- [21] B. Goyal, A. Dogra, S. Agrawal, B.S. Sohi, and A. Sharma. Image denoising review: From classical to state-of-the-art approaches. *Information Fusion*, 55:220–244, 2020.
- [22] S. Gu, L. Zhang, W. Zuo, and X. Feng. Weighted nuclear norm minimization with application to image denoising. In *2014 IEEE Conference on Computer Vision and Pattern Recognition*, pages 2862–2869, 2014.
- [23] B. Han, Q. Mo, Z. Zhao, and X. Zhuang. Directional compactly supported tensor product complex tight framelets with applications to image denoising and inpainting. *SIAM J. Imaging Sci.*, 12(4):1739–1771, 2019.
- [24] B. Han and Z. Zhao. Tensor product complex tight framelets with increasing directionality. *SIAM J. Imaging Sci.*, 7(2):997–1034, 2014.
- [25] B. Han, Z. Zhao, and X. Zhuang. Directional tensor product complex tight framelets with low redundancy. *Appl. Comput. Harmon. Anal.*, 41(2):603–637, 2016.
- [26] A. E. Ilesanmi and T. O Ilesanmi. Methods for image denoising using convolutional neural network: a review. *Complex Intell. Syst.*, 7:2179–2198, 2021.
- [27] A. Jalobeanu, L. Blanc-Féraud, and J. Zerubia. Satellite image deconvolution using complex wavelet packets. In *Proc. IEEE Int. Conf. Image Process. (ICIP)*, pages 809–812, 2000.
- [28] H. Ji, Z. Shen, and Y. Zhao. Directional frames for image recovery: Multi-scale discrete Gabor frames. *Journal of Fourier Analysis and Applications*, 23(4):729–757, 2017.
- [29] H. Ji, Z. Shen, and Y. Zhao. Digital Gabor filters with MRA structure. *SIAM Journal on Multiscale Modeling and Simulation*, 16(1):452–476, 2018.
- [30] N.G. Kingsbury. Image processing with complex wavelets. *Philos. Trans. R. Soc. London A, Math. Phys. Sci.*, 357(1760):2543–2560, 1999.
- [31] G. Kutyniok and D. Labate. *Shearlets: Multiscale Analysis for Multivariate Data*. Birkhäuser, Boston, 2012.

[32] Xiaoxia Li, Juan Xiao, Yingyue Zhou, Yuanzheng Ye, Nianzu Lv, Xueyuan Wang, Shunli Wang, and ShaoBing Gao. Detail retaining convolutional neural network for image denoising. *Journal of Visual Communication and Image Representation*, 71:102774, 2020.

[33] J. Liu and S. Osher. Block matching local SVD operator based sparsity and TV regularization for image denoising. *Journal of Scientific Computing*, 78:607–624, 2019.

[34] Chong Mou, Jian Zhang, Xiaopeng Fan, Hangfan Liu, and Ronggang Wang. Cola-net: Collaborative attention network for image restoration. *IEEE Transactions on Multimedia*, 24:1366–1377, 2022.

[35] Yuhui Quan, Yixin Chen, Yizhen Shao, Huan Teng, Yong Xu, and Hui Ji. Image denoising using complex-valued deep cnn. *Pattern Recognition*, 111:107639, 2021.

[36] Y. Romano and M. Elad. Boosting of image denoising algorithms. *SIAM J. IMAGING SCIENCES*, 8(2):1187–1219, 2015.

[37] I.W. Selesnick, R.G. Baraniuk, and N.G. Kingsbury. The dual-tree complex wavelet transform. *IEEE Signal Process. Mag.*, 22(6):123—151, 2005.

[38] L. Šendur and I. Selesnick. Bivariate shrinkage with local variance estimation. *IEEE Signal Process. Letters*, 9(12):438–441, 2002.

[39] Wuzhen Shi, Feng Jiang, Shengping Zhang, Rui Wang, Debin Zhao, and Huiyu Zhou. Hierarchical residual learning for image denoising. *Signal Processing: Image Communication*, 76:243–251, 2019.

[40] Pham Huu Thanh Binh, Cristóvão Cruz, and Karen Egiazarian. Flashlight CNN image denoising. In *2020 28th European Signal Processing Conference (EUSIPCO)*, pages 670–674, 2021.

[41] Chunwei Tian, Lunke Fei, Wenxian Zheng, Wangmeng Zuo Yong Xu and, and Chia-Wen Lin. Deep learning on image denoising: An overview. *Neural Networks*, 131, 2020.

[42] Z. Wang and A. C. Bovik. Mean squared error : Love it or leave it? *IEEE Signal Process. Mag.*, 26:98–117, January 2009.

[43] Z. Wang, A. C. Bovik, H. R. Sheikh, and E. P. Simoncelli. Image quality assessment: From error visibility to structural similarity. *IEEE Trans. Image Proc.*, 13(4):600–612, 2004.

[44] Y. Hou and D. Shen. Image denoising with morphology- and size-adaptive block-matching transform domain filtering. *EURASIP Journal on Image and Video Processing*, 59, 2018.

[45] K. Zhang, W. Zuo, Y. Chen, D. Meng, and L. Zhang. Beyond a Gaussian denoiser: residual learning of deep CNN for image denoising. *IEEE Trans. Image Process.*, 26(7):3142–3155, 2017.

[46] T. Zhou, C. Li, X. Zeng, and Y. Zhao. Sparse representation with enhanced nonlocal self-similarity for image denoising. *Machine Vision and Applications*, 32(5):1–11, 2021.

- [47] X. Zhuang. Digital affine shear transforms: fast realization and applications in image/video processing. *SIAM J. Imag. Sci.*, 9(3):1437–1466, 2016.
- [48] X. Zhuang and B. Han. Compactly supported tensor product complex tight framelets with directionality. In *2019 International Conference on Sampling Theory and Applications (SampTA), Bordeaux, France*.